File LockwoodandMcWilliams_2001_S1.doc
11th May 2021
submitted to: J. Geophys. Res.

A survey of 25 years' transpolar voltage data from the SuperDARN radar network and the Expanding-Contracting Polar Cap model

Mike Lockwood[1] and Kathryn A. McWilliams[2]

[1] *Department of Meteorology, University of Reading, Earley Gate, Reading, RG6 6BB, UK*

[2] *Institute of Space and Atmospheric Studies, University of Saskatchewan, Saskatoon, Saskatchewan, Canada*

Abstract. We use 214410 hourly observations of the transpolar voltage, Φ_{PC}, from 25 years' observations by the SuperDARN radars to confirm the central tenet of the Expanding-Contracting Polar Cap model of ionospheric convection that Φ_{PC} responds to both dayside and nightside reconnection voltages (Φ_D and Φ_N). We show Φ_{PC} increases at a fixed level of nightside auroral electrojet *AL* index with increasingly southward IMF (identifying the well-known effect of Φ_D on Φ_{PC}) but also with increasingly negative *AL* at a fixed southward IMF (identifying a distinct effect of Φ_N on Φ_{PC}). We study the variation of Φ_{PC} with time elapsed since the IMF last pointed southward and show that low/large values occur when $(-AL)$ is small/large. We have to allow for the fact that at lower numbers of radar echoes, n_e, the "matched potential" re-analysis technique used to derive Φ_{PC} is influenced by the model used: this is done by a sensitivity study of the threshold of n_e required. We show that for any threshold n_e, Φ_{PC} falls to about 15kV for Δt greater than about 15 hours giving an upper limit to the viscous-like voltage Φ_V. It is shown that both Φ_{PC} and $(-AL)$ increase with increased solar wind dynamic pressure p_{SW}, but not as much as mid-latitude geomagnetic range index am. We conclude p_{SW} increases both Φ_D and Φ_N through increasing the magnetic shear across the relevant current sheet but has a bigger effect on mid-latitude geomagnetic activity indices via the additional energy stored in the tail lobes.

1. Introduction.

One aim of this paper is to re-create two scatter plots from surveys of the ionospheric transpolar voltage, Φ_{PC}, (a.k.a. the cross-cap potential difference) that have been of great importance to our understanding of the excitation of ionospheric polar convection by the solar wind flow, but here using a very much larger dataset of observations. We also aim to use the large dataset, which covers more than whole Hale solar magnetic cycle, to extend our understanding of the separate effects of reconnection in the magnetopause and the cross-tail current sheet by comparisons with the behaviour of the AL auroral electrojet index.

1-i. Transpolar voltage, steady state and non-steady-state convection

Magnetospheric convection (the circulation of plasma and frozen-in magnetic field) is at the heart of our understanding of the response of geomagnetic activity and terrestrial space weather to the transfer of energy from the solar wind. Directly-driven geomagnetic responses (historically called "Disturbance Polar-2" or "DP-2") correlate highly with solar wind forcing with short response delay (*Nishida,* 1968a; b; *Lockwood et al.,* 1986; *Etemadi et al*., 1988; *Todd et al.,* 1988). These are driven responses to magnetic reconnection in the dayside magnetopause current sheet which generates open magnetospheric field lines (*Consolini and De Michelis*, 2005; *Finch et al.*, 2008; *Echer et al.,* 2017). The open field lines generated are swept into the geomagnetic tail by the solar wind flow where they accumulate, storing energy there. These open field lines in the tail are subsequently re-closed in bursts of reconnection in the cross-tail current sheet, giving the storage-release responses of geomagnetic activity ("DP-1") after a longer lag time (*Baker et al.,* 1983; *McPherron et al.,* 1998; *Klimas et al.,* 1992; 1994; *Finch et al.,* 2008). The storage-release response is often described in terms of the magnetospheric substorm cycle (e.g., *Baker et al.,* 1997; *McPherron et al.,* 1998). A review of the development of our understanding of the relationship of magnetospheric flux transport, the Dungey convection cycle and substorms has been given by *McPherron* (2020) and a review of the associated energy flow through the magnetosphere has been given by *Lockwood* (2019).

Being at the foot of magnetospheric field lines and, like the magnetosphere, being of high magnetic Reynolds number, the frozen-in flux theorem applies in the F-region and topside ionosphere. Hence these regions reflect the circulation of frozen-in flux in the magnetosphere (ionospheric convection). However, there is one key difference between the magnetosphere

and the ionosphere: whereas the magnetosphere is compressible (indeed the storage-release system depends on that fact), the ionosphere is incompressible, in the sense that the magnetic field there is constant to within a very small factor (even a very large 1000nT geomagnetic disturbance is less than a 2% perturbation). The reason for this is the ionosphere's close proximity to the currents in the Earth's interior that generate the geomagnetic field. This difference means that during substorm growth phases, when energy is accumulating in the near-Earth lobes of the magnetospheric geomagnetic tail because the field there is growing (and to some extent the lobes are expanding in size as the tail flares), the ionospheric footprint of the open field lines of the lobes (the open polar caps) must be expanding in area (*Holzer et al.*, 1986; *Lockwood et al.,* 1990; *Lockwood and Cowley,* 1992, *Milan et al*., 2003; 2009; 2012; *Huang et al.*, 2009). *Siscoe and Huang* (1985) showed how expanding "adiaroic" segments polar cap boundaries (meaning "not flowing across", i.e., not mapping to a magnetospheric reconnection site) would influence the pattern of ionospheric convection. This concept was used by *Cowley and Lockwood* (1992) to show how ionospheric convection is driven by both the generation and destruction of open flux (the "Expanding-Contracting Polar Cap", ECPC model) whereas in the magnetosphere flows are driven by the solar wind flow, pressure balance and the magnetohydrodynamic (MHD) curvature force that acts to straighten bent field lines. The concept is supported by detailed comparisons between theory and observations of how patches of newly opened flux generated by magnetopause reconnection bursts evolve poleward (*Cowley et al.,* 1991; *Lockwood et al.*, 1993; *McWilliams et al*., 2000; *Throp et al*., 2005; *Lockwood et al.,* 2006). As a result, ionospheric convection is not, in general, a straightforward image of the magnetospheric circulation and the two are decoupled by induction effects – changes in the magnetic field between the magnetosphere and the ionosphere which, by Faraday's law, give a curl in the electric field (*Lockwood et al*., 1990; *Lockwood and Cowley,* 1992; *Lockwood and Morley*, 2004). In steady-state, the electric field becomes curl-free and electrostatic potentials do map down magnetic field lines; in addition, in steady state adiaroic boundaries are not moving and so the ionospheric convection pattern does become an image of the magnetospheric circulation. Steady-state applies when we average data over a long enough timescale but does not apply to the timescales of a few substorm cycles and less. That is not to say that balanced reconnection events, when dayside and nightside reconnection voltages are approximately equal, do not occur (*DeJong et al.,* 2008, *Lockwood et al*., 2009): these can occur by chance but probably

more often because the growth of the dayside reconnection voltage is slow, such that it is never greatly different to the lagged nightside voltage response (*Milan et al*., 2021). Surveys by *Lockwood et al.* (2009) and *Milan et al.* (2021) have looked at the relative occurrence of substorm cycles and quasi-balanced reconnection. Note that the ECPC model is the general case as it can predict quasi-steady quasi-balanced reconnection (if the interplanetary condition drivimg dayside reconnection vary slowly enough) as well substorm cycles, but balanced reconnection is not the general case as it cannot predict substorm cycles (nor is there any known mechanism that can balance the reconnection rates at any one instant). *Lockwood* (1991) pointed out that the motion of adiaroic convection reversals boundaries means that they are smoothed out in average patterns of convection. On timescales shorter than the substorm cycle of polar cap expansion and contraction, ionospheric convection reflects both the DP1 and DP2 current systems and displays the response delays associated with both (respectively a few minutes and 30-60 min). In addition, because of a combination of ionospheric incompressibility and the antisunward motion of open field lines, the response delay varies with location, increasing with distance away from noon (*Lockwood et al.*, 1986; *Saunders et al.*, 1992; *Lopez et al.*, 1999; *Morley and Lockwood*, 2005).

Convection is often quantified by the transpolar voltage Φ_{PC} between convection reversal boundaries in the ionosphere on the dawnside and the duskside of the polar cap (*Reiff et al*., 1981; *Cowley*, 1984*; Weimer et al.*, 1990; *Boyle*, 1997; *Hairston et al*., 1998). This parameter is measured by Low-Earth Orbit (LEO) spacecraft by integration of the observed along-track component of the electric field along the satellite path between the two dominant Convection Reversal Boundaries (CRBs). That electric field can be either directly measured or derived from observations of the vector magnetic field, $\vec{B}$ and the plasma flow $\vec{V}$ and using the equation of ideal MHD $\vec{E} = -\vec{V}\times\vec{B}$ which applies to a very high degree of accuracy even in the F-region ionosphere (*Hanson et al.*, 1994). Hence by integrating the along-track electric field (corresponding to the cross-track drift) between the two main CRBs, the transpolar voltage Φ_{PC} is measured for that satellite path. The quantity Φ_{PC} is often accurately called the "polar cap potential drop", but also frequently (but inaccurately) referred to as the "cross-cap potential" or "polar cap potential". Strictly-speaking, it is a potential difference, i.e., a voltage, and this semantic point has real physical significance to understanding because, by Faraday's induction law, a voltage is synonymous with magnetic flux transfer rate whereas a potential is not. Hence, we here use the term "transpolar voltage" for Φ_{PC} and note it is the

rate at which magnetic flux is transferred across the polar cap. One convention that is used is that positive Φ_{PC} is the dawnside CRB potential exceeds the duskside CRB potential (i.e., the electric field is from dawn to dusk), and this applies most of the time because net flux transfer is from the dayside to nightside. The reason for this is that open flux is, by definition, embedded in the solar wind flow and the solar wind is always transferring that open flux antisunward and, during even the longest intervals of northward IMF, the open flux never decays away. In terms of magnetospheric configuration and voltages, this means the geomagnetic tail is always present and so magnetic shear is always present between the two tail lobes and gives magnetic reconnection in the associated cross-tail current sheet. In addition, reconnection in the dayside magnetopause between the magnetic cusps that opens geomagnetic field lines has been observed to continue (at a low level) even during intervals of northward IMF (*Chandler et al*., 1999; *Fuselier et al.*, 2000).

If Φ_{PC} is defined as dawn the potential minus the dusk potential, the presence of lobe reconnection during northward IMF can give sunward flow in the polar cap and negative values if that reconnection causes a larger voltage in the ionosphere than the combined anti-sunward flow effect of non-reconnection processes "viscous-like interactions" and the residual effect of nightside reconnection. Note that this means that the voltage can flip suddenly from positive to negative because of a small increase in the lobe reconnection voltage that raises it above that threshold. It is important to note that we do not here use this definition of Φ_{PC}, rather we take it to be the largest potential difference present and so it is always a positive number.

The presence of lobe stirring cells during northward IMF, or even lobe field line re-closure by reconnection at the sunward edges of both lobes (e.g. *Lockwood and Moen*, 1999), means that northward IMF is inherently a non-steady-state situation because, by Faraday's law, the electric field has a curl with dawn-to-dusk electric field associated with reconnection in the cross-tail current sheet but dusk-to-dawn electric field along the reconnection site(s) at the sunward edge(s) of the lobe magnetopause (*Lockwood*, 2019). Hence during the 50% of time that the IMF points northward (*Hapgood et al*., 1991; *Lockwood et al.*, 2017; 2019b) the magnetosphere is quiet but also inherently in a non-steady state because of the slow decay of open flux (see review by *Lockwood*, 2019).

Milan et al. (2021) surveyed one-year of data and found that roughly 20% of all antisunward magnetospheric flux transfer was during quiet periods, 43% during non-steady-state phases (20.8% substorm growth, 9.8% substorm expansion, 3.3% substorm recovery, 1.2% recovery bays and 8% multiple intensifications). The remaining 37% was during intervals they classed as "driven" – these include extended substorm growth phases and periods when dayside and nightside reconnection are close to being balanced ($\Phi_D \approx \Phi_N$). This driven state was found for 18.2% of the time, compared to 27.2% of the time for the non-steady phases (together these making up the 50% of time that the IMF points southward). Hence in both time and resulting flux transfer non-steady conditions was the dominant magnetospheric response. However, we introduce steady state into our view of the magnetosphere or ionosphere at all times if we average data together. In steady-state, the rate of flux transfer across the polar cap, Φ_{PC} equals the rate at which field lines are opened by reconnection in the dayside magnetopause (the dayside reconnection voltage Φ_D) and the rate at which open field lines are closed by reconnection in the cross-tail current sheet (the nightside reconnection voltage Φ_N), plus any non-reconnection "viscous-like" voltage, Φ_V (i.e. $\Phi_{PC} = \Phi_D + \Phi_V = \Phi_N + \Phi_V$). At the nightside reconnection site there can be no information about the instantaneous value of Φ_N, at the dayside reconnection site, and so $\Phi_D \approx \Phi_N$, is not going to happen as a matter of course and Faraday's law applied to the open-closed field line boundary gives the general behaviour:

$$dF_o/dt = B_i . dA_o/dt = \Phi_D - \Phi_N \qquad (1)$$

where W_o is the open magnetospheric flux, A_o the area of the open field line polar cap in the ionosphere and B_i is the magnitude of the field in the ionosphere. (Note that Equation (1) can be thought of as the continuity equation for the open flux F_o). Hence steady state requires $\Phi_D = \Phi_N$ and $dF_o/dt = dA_o/dt = 0$. The results of *Lockwood et al.* (2009) and *Milan et al.* (2021) show that non-steady state is a common situation, which is to be expected because of the variability in the IMF orientation (and hence Φ_D) and the fact that the transfer of information from the dayside magnetopause reconnection site to that in the cross-tail current sheet takes time and hence Φ_N can only respond after a lag. How common balanced convection ($\Phi_D \approx \Phi_N$) events are is a matter of definition (see *McWilliams et al.*, 2008) and they will be less common if tighter limits placed on the maximum ($\Phi_D - \Phi_N$) used to define

them. For a large averaging timescale τ the time derivatives in equation (1) tend to zero because long-term trends in F_o and A_o are negligibly small. So, for large enough τ

$$< \Phi_{PC} >_\tau - < \Phi_V >_\tau = < \Phi_D >_\tau = < \Phi_N >_\tau \qquad (2)$$

even though this condition only applies relatively rarely at any one instant of time during southward IMF.

The voltage Φ_V is generated by any non-reconnection process transferring momentum from the flow of the shocked solar wind in the magnetosheath to closed field lines (e.g., *Farrugia et al*., 2001). The ECPC model predicts that Φ_V is small and that most of what had previously been thought to be voltage driven by viscous-like processes is, in fact, due to the nightside reconnection voltage Φ_N which always persists because the geomagnetic tail never erodes away and so there is always magnetic shear in the centre of the tail (*Wygant et al.*, 1983, *Lockwood et al.*, 1990; *Lockwood*, 1991; *Milan*, 2004). Numerical simulations have confirmed that Φ_N contributes to transpolar voltage Φ_{PC} in addition to Φ_N (e.g., *Gordeev et al.*, 2011).

Lockwood (1991) pointed out that value of Φ_{PC} for a given Φ_D, Φ_N and Φ_V will depend on the shape of the open polar cap and how it is changing and only for an open polar cap that remains circular at all times does $\Phi_{PC} = \Phi_V + (\Phi_D + \Phi_N)/2$. Hence, in general for the duration of each polar cap traversal by a LEO satellite we have to consider non-steady conditions, and that each Φ_{PC} value observed will depend on Φ_D, Φ_N, and Φ_V and on how the polar cap is changing shape (i.e., the motion of the adiaroic boundaries which reflect the potential distribution along the boundary) and, critically, on the satellite path. Passes of the dayside polar cap will reflect the influence of Φ_D to greater extent and for passes over the nightside polar cap the influence of Φ_N will be greater.

The question then arises what is the minimum averaging timescale τ is required to make equation (2) apply to a good approximation? Clearly, τ smaller than about 3 hours is inadequate as it is comparable to the timescales of the substorm cycle over which the open polar cap expands and contracts. *Imber et al.* (2013) show that over the sunspot cycle the polar cap area is remarkably constant (i.e., dF_o/dt is negligible) over timescales τ of order years. Both modelling (e.g., *Lopez et al.*, 2001) and observational studies (e.g., *Mishin and Karavaev*, 2017) show that F_o rises during the initial phases of large geomagnetic storms but

F_o, like Φ_{PC} (e.g., *Kubota et al.*, 2017), appears to saturate establishing a temporary quasi-steady state, before falling again as the storm declines. These "Balanced Reconnection Intervals" are related to the phenomenon of "Steady Magnetospheric Convection" (SMC) (*McWilliams et al.*, 2008) events but do not necessarily start with a substorm growth phase nor end with a substorm expansion phase (*DeJong et al.*, 2008); however, because in general there is a long-term variation in F_o around both BRI and SMC events they cannot be considered a steady-state phenomenon on timescales shorter than their duration. (Although we note that some BRI and SMC events probably can occur without prior of subsequent major change in F_o via chance occurrences of matched Φ_N and Φ_D variations or because the rate of change in Φ_D has been slow). Hence, in general, we need τ to exceed storm durations for steady state to fully apply. *Haines et al.* (2019) have surveyed geomagnetic storms in the homogeneous aa index, aa_H (*Lockwood et al.*, 2018a; b) since 1868, defining storms as when aa_H exceeded its overall 90th percentile: of the 10^4 storms defined by this threshold, none lasted more than 3 days. Hence $\tau \geq 3$ days should generally make steady-state a valid assumption. Note that *Weigel* (2007) proposes that the time constant is considerably longer than this, such that non-steady conditions even influence the variation with time of year; however, as demonstrated by *Lockwood et al.* (2016), this would generate an "axial-like" time-of-day/time-of-year pattern and we can discount this proposal.

1-ii. SuperDARN Tranpolar Voltage Data

The studies of transpolar voltage discussed in the previous section were made using observations of electric fields and plasma flows by LEO satellites as they passed over the polar caps. One problem with this is that the satellite path will not generally intersect the points of maximum and minimum potential and so the difference between them, the transpolar voltage Φ_{PC}, will be systematically underestimated. In addition, because there is no information of the potential pattern away from the satellite path, there is no way of checking if, or by how much, any one value is an underestimate. Studies have generally used passes that are close to the dawn-dusk meridian to try to minimise this problem, but the ECPC model predicts that this will only work for steady state conditions. This is because for dominant magnetopause reconnection ($\Phi_D > \Phi_N$), both the maximum and minimum of the potential pattern will be shifted towards noon and for dominant tail reconnection ($\Phi_N > \Phi_D$) they are shifted towards midnight. In this paper we use values derived from the SuperDARN coherent

radar arrays. By imaging the convection pattern, the points of maximum and minimum potential can be identified and the problem inherent in the spacecraft data avoided. However, there are some other important points to note about the transpolar voltage data from the SuperDARN radars.

The radars monitor the line-of-sight component of the flow of F-region plasma by measuring the Doppler shift of coherent echoes reflected off convecting ionospheric irregularities embedded in the bulk plasma flow. The most accurate method for generating two-dimensional field-perpendicular convection velocity vectors from the SuperDARN radar data is by combining the line-of-sight measurements within a common field-of-view of a pairs of radars (e.g., *Greenwald et al.*, 1995). However, because of the aspect sensitivity of echoes with respect to the structures causing the scatter, for much of the time when echoes are recorded by one radar, they are not detected by the twin radar looking in a different direction and so opportunities to make these "bistatic" observations are relatively rare. Hence methods to find the functional form for the distribution of electrostatic potential that was a best fit to all the line-of-sight velocity measurements were developed (*Ruohoniemi and Baker*, 1998; *Cousins et al.*, 2013). The most widely used of these is the "Map-Potential" technique (a form re-analysis using data-assimilation), which performed well when tested against available bistatic vectors (*Provan et al.*, 2002). However, lack of radar coverage and/or of the required scattering irregularities mean that line-of-sight data are not available at all locations in the polar regions and so the velocity data are supplemented with data from a statistical model, driven by the IMF conditions observed by an upstream monitor. From each derived map-potential pattern the transpolar voltage Φ_{PC} can be scaled (*Bristow et al.*, 2004; *Wilder et al.*, 2011). A review of the development and application of this technique has been presented by *Chisham et al.* (2007).

The model data used in the map-potential technique are weighted to minimize the impact of the statistical model for a given number of available radar echoes, n_e (*Shepherd and Ruohoniemi*, 2000). At times there are sufficient numbers and distribution of echoes for the potential pattern to be determined from the radar data alone; on the other hand, in extreme cases with no echoes ($n_e = 0$), the pattern is determined purely by the model which is driven by the observed upstream interplanetary conditions. Tests of flow velocities derived using the SuperDARN radars have been made by comparing the map-potential flow estimates with data

from the DMSP (e.g., *Xu et al.*, 2007a; b; *Drayton et al*., 2005) and SWARM (*Koustov et al.*, 2019a) spacecraft. In addition, transpolar voltage data from the SuperDARN map-potential data have been compared to those derived by the AMIE (Assimilative Mapping of Ionospheric Electrodynamics) technique that uses a variety of sources, particularly magnetometers (*Gao*, 2012). Given that there is a tendency for flow speeds defined by SuperDARN to be about 30% lower than seen by satellites (*Xu et al*., 2007b; *Drayton et al.*, 2005; *Koustov et al*., 2019a), but that convection reversal boundary locations in the two data sets are very similar, we would expect SuperDARN values of Φ_{PC} to be well correlated with the satellite values but typically 30% lower. In this paper we use a variety of threshold values of n_e, n_{min} to investigate the effect of low n_e on our results. All Φ_{PC} values based on $n_e <$ n_{min} echoes were discarded and we varied n_{min} to determine the sensitivity of our results to the choice of n_{min}.

The use of a $n_e > n_{min}$ selection criterion has an important but subtle implication for biases in the data because considerably fewer echoes are received during summer. This is probably due to combination of causes acting together including: sporadic E-blanketing of F-region radar returns; interference from enhanced ground echoes; a smother ionosphere when photoionization rate is high and the transmitter frequency selection (*Koustov et al.*, 2019b and references therein). We here use only maps from the northern hemisphere radar array with its greater number of stations and the means of n_e are consistently about 200 around the June solstice (summer) whereas they are typically between 500 and 600 around the December (solstice) winter. This means that summer hourly values that meet, for example, a $n_e > n_{min} = 255$ criterion are rare in summer and atypical (around 2-3 per day, whereas there are 20-24 per day in winter).

The other factor that we need to be aware of is that the occurrence of echoes also increases with the plasma velocity (*Koustov et al.*, 2019b). This means that although we want to avoid samples with low n_e to minimise the role that the data-assimilation convection model plays in the Φ_{PC} value, we do not want to eliminate too many samples because that would preferentially remove low flow (and hence low Φ_{PC}) samples.

The ECPC model has been used to quantitatively match to map-potential SuperDARN observations of the evolution of the convection pattern and Φ_{PC} following individual events

of southward and northward turnings if the IMF (*Lockwood et al.*, 2006), events that were also quantitatively compared to the associated signatures of magnetopause reconnection in cusp proton precipitation and aurora (*Lockwood et al.*, 2003; *Throp et al.*, 2005). Here we make a statistical study of the Φ_{PC} data from SuperDARN using data from 25 years – more than a full Hale solar magnetic cycle.

2. Data Employed

In this paper we make use of 214410 hourly observations of the ionospheric transpolar voltage, Φ_{PC}, derived from 25 years of observations by the SuperDARN radar network (1995-2020). These data are generated using the map-potential technique in 2-minute integration periods and the 30 values of Φ_{PC} and n_e in each hour were then averaged together. It is important to note that we define Φ_{PC} as the maximum potential difference between any two points in the potential pattern. Hence both subsolar and lobe reconnection, driving antisunward and sunward flow respectively (e.g., *Lockwood and Moen*, 1999), can contribute to positive Φ_{PC}. The processed data have been checked and calibrated using comparisons with dawn dusk passes by Defense Meteorological Satellite Program (DMSP) satellites from 2001-2002 for which the SuperDARN convection patterns show potential minima and maxima close to the satellite path.

We compare with data on the north-south component of the Interplanetary Magnetic Field (IMF) (in the Geocentric Magnetospheric Reference frame, B_Z) and the solar wind dynamic pressure (p_{SW}) taken from the Omni dataset, compiled and maintained by NASA's Goddard Space Flight Center. We also compare with the AL auroral electrojet geomagnetic index compiled and maintained by the World Data Centre for Geomagnetism, Kyoto. We use one-minute values of B_Z, p_{SW} and AL. Because we are not sure of the precise propagation lags of these parameters relative to the Φ_{PC} data we take running (boxcar) means over a timescale τ which we then interpolate to the mid-point of the hour over which Φ_{PC} data are averaged, minus a nominal lag δt. We repeated all studies using two values of τ, $\tau = 1hr$ to match the averaging timescale of the Φ_{PC} data and $\tau = 15min.$: plots for the two were almost identical and we use $\tau = 15min.$ in the plots shown. For IMF B_Z we use a lag $\delta t = 5\ min.$, to allow for propagation across the magnetosheath to the dayside magnetopause reconnection line and then down geomagnetic field lines to the ionosphere, because we are interested in the effect of

IMF B_Z on the dayside reconnection voltage, Φ_D. For p_{SW} we have tried try two different values of δt: to search for an effect of p_{SW} on Φ_D we use $\delta t = 5min$ as for IMF B_Z, and to search for an effect of p_{SW} on Φ_N we use $\delta t = 75min$ (derived below). The latter effect is expected from squeezing of the near-Earth tail, as recently observed and modelled by *Lockwood et al.* (2020a;b; 2021). Because of the persistence in the p_{SW} data sequence the results are similar for the two δt values, however somewhat clearer effects are seen for $\delta t =$ 75 min. and that is the value employed in the plots presented. For AL, we use $\delta t = 0$ as both AL and the Φ_N value are used as an indicator of signatures in the nightside auroral ionosphere. We compute $p_{SW} = m_{SW} N_{SW} V_{SW}^2$ from 1-minute values of the solar wind mean ion mass m_{SW}, number density N_{SW} and speed V_{SW}; in the case of m_{SW} these are linearly interpolated from 5 min., 15 min or hourly observations if 1-min. values are unavailable.

3. Results

3-i. Effect of number of radar echoes, n_e

Figure 3 shows the cumulative probability distribution (c.d.f.) of the number of radar echoes n_e for the 214410 samples of the ionospheric transpolar voltage, Φ_{PC}. The vertical coloured lines show a set of nominal values of n_{min}, which we vary from 100 (dark red) to 900 (mauve) in steps of 100 in our sensitivity study. These values yield subsets of 137633, 85078, 52501, 32646, 20378, 12866, 8032, 4958, and 3134 samples. The black dashed line is for n_{min} = 255 which we discuss below and which yields 60653 samples, very close to 30% of the original dataset.

Figure 4 shows the probability distribution functions for hourly transpolar voltage, Φ_{PC}, selected using the condition $n_e > n_{min}$ for these values of for n_{min}. It can be seen that the shape of the distribution varies with n_{min} with the mode value of the normalised distribution getting smaller and moving to higher values and the large-value tail gets relatively larger, as expected from the discussion in section 1-ii. It can be seen that for n_{min} < 300 the effect is, however, relatively minor.

To further define an optimum value for n_{min} we have carried out a comparison with dawn-dusk passes by DMSP satellites for the years 2001 and 2002 and compared the transpolar voltage derived, $[\Phi_{PC}]_{\mathrm{DMSP}}$, with the simultaneous SuperDARN map-potential estimates,

$[\Phi_{PC}]_{\text{S.DARN}}$. We computed the root mean square deviation, $(< \Delta\Phi_{PC}^2 >)^{1/2}$ (where $\Delta\Phi_{PC} = [\Phi_{PC}]_{\text{DMSP}} - [\Phi_{PC}]_{\text{S.DARN}}$) as a metric of agreement. In general, we found $\Delta\Phi_{PC}$ tended to be positive, consistent with the studies discussed in section 1-ii. We used the Nelder-Mead search to find a minimum in $(< \Delta\Phi_{PC}^2 >)^{1/2}$ as a function of n_{min} and the maximum allowed geocentric angular separation of the satellite and radar potential maxima and minima, δ. This yielded an optimum n_{min} of 255 and for the optimum maximum δ of 30° the use of n_{min} = 255 gave a peak correlation between $[\Phi_{PC}]_{\text{DMSP}}$ and $[\Phi_{PC}]_{\text{S.DARN}}$ of 0.85 with and r.m.s. deviation $(< \Delta\Phi_{PC}^2 >)^{1/2} = 18.5kV$, compared to a correlation of 0.82 for $n_{min} = 0$, for which $(< \Delta\Phi_{PC}^2 >)^{1/2} = 21.2kV$. Hence agreement was most improved by adopting of n_{min} = 255 which is a value small enough not to greatly change the shape of the overall distribution of $[\Phi_{PC}]_{\text{S.DARN}}$ values, as shown by Figure 4. We also used this survey to calibrate the SuperDARN estimates: the systematic underestimation of the SuperDARN values was corrected in the entire 1995-2020 dataset using the linear regression of the $[\Phi_{PC}]_{\text{DMSP}}$ and $[\Phi_{PC}]_{\text{S.DARN}}$ data for n_{min} = 255 and $\delta <$ 30°.

In sections 3-ii to 3-iv of this paper we employ the selection criterion $n_e > n_{min}$ = 255 (which gives us 60653 samples). However, we do return to using all the n_{min} values in section 3-v in a sensitivity study to show that our conclusions are not influenced by the value of n_{min} adopted.

3-ii. Variation of Φ_{PC} with IMF B_Z and the AL index

Figure 5 analyses the optimum propagation lags needed for this study. The black line is the lag correlogram (linear correlation coefficient as a function of lag) for Φ_{PC} and the IMF $-B_Z$ (in the GSM frame). The peak correlation is with Φ_{PC} lagging behind B_Z by δt = 20 min. This is longer than the response time for dayside magnetopause reconnection: from the propagation delay to cross the magnetosheath this is expected to be about 5 min. which is the typical response time seen in the observational studies discussed in section 1-i. The propagation of the enhancement to the centre of the polar cap was modelled using the ECPC model by *Morley and Lockwood* (2005) and a value of 20 minutes from nose of the bow shock is broadly consistent with their predictions. If we limit the dataset to times of low nightside activity by requiring that the AL index be above 100 nT ($-AL < 100nT$, the blue line), the ECPC convection model predicts that the transpolar voltage will appear across the

dayside region merging gap at such times (with $\Phi_{PC} \approx \Phi_D + \Phi_V$) and the observed lag of Φ_{PC} lag after B_z of $\delta t = 5\ min$ for this subset is consistent with this. A notable feature of all the correlograms in Figure 5, except those for Φ_{PC} and B_z (in blue and black), is that correlations are higher after the peak than before it. This shows that higher auroral activity (larger negative AL) are responses over longer timeconstants. The orange line shows that the optimum lag for the AL index after B_z is $\delta t = 35\ min$, but the peak is lower and broader indicating there is considerable variability in that lag. The green line gives the lag of the AL index after Φ_{PC} of $\delta t = 25\ min$, which yields a total lag of 25+20 = 45 min after IMF B_z which is 10 min longer than the value obtained from the direct correlation between AL and IMF B_z. The mauve line shows the correlation between Φ_{PC} and solar wind dynamic pressure p_{SW} which is considerably weaker, as expected because Φ_{PC} depends primarily on Φ_D and Φ_N which are not expected to be as strongly modulated by p_{SW} as they are by B_z. However, this Φ_{PC} versus p_{SW} correlogram does show a broad, weak peak with a maximum at a lag of $\delta t = 120\ min$. This suggests that if p_{SW} is exerting an influence on Φ_{PC} it is mainly via a modulation of Φ_N through squeezing the near-Earth cross-trail current sheet. This will be discussed further in section 3-iii. The correlation between Φ_{PC} and p_{SW} was also examined for northward and southward IMF conditions separately by selecting data when the B_z data simultaneous with p_{SW} was positive and negative, giving the cyan and grey correlograms, respectively. For southward IMF the peak effect is soon after that of the peak response to IMF B_z and so this appears to show an influence of p_{SW} on the dayside reconnection voltage Φ_D. On the other hand, the peak response for northward IMF is at a lag of $\delta t = 75\ min$. and because of the absence of large Φ_D in these cases, this appear to show a response of Φ_N to increased p_{SW} in these cases (see discussion by *Lockwood*, 2013). In our studies we used δt of 5, 75 and 120 min. for the optimum lag between p_{SW} and terrestrial responses: because of the high persistence in the p_{SW} data series the results were very similar in the three cases and we here show values for $\delta t = 75 min$.

A great many studies have presented scatter plots of Φ_{PC} as a function IMF B_Z (or dawn-dusk interplanetary electric field $V_{SW}B_Z$, but the radial solar wind speed V_{SW} explains very little of the scatter) and shown that Φ_{PC} increases approximately linearly with $-B_Z$ for $B_Z < 0$ but has approximately constant and small values for $B_Z > 0$. Figure 6 shows that the SuperDARN data also confirms this behaviour. Because there are so many samples in our

study, a scatter plot loses a great deal of information because so many points are plotted on top of each other. Hence in Figure 6 we color-code the fraction of samples ($n/\Sigma n$, on a logarithmic scale) in bins of narrow width in both Φ_{PC} and B_Z. The bins used are $\Delta B_z = 0.5nT$ wide in IMF B_z and $\Delta\Phi_{PC} = 2\ kV$ wide in the Φ_{PC}. The plot shows the features that are familiar from other plots (compare, for example, with the plot for 60 data points from polar passes by 4 satellites by *Cowley*, 1984). Two important features to note are that: (1) for southward IMF there is a considerable spread in Φ_{PC} at a given B_z; and (2) for northward IMF that spread decreases with increasingly positive B_z. The also plot shows that Φ_{PC} values increase slightly with increasingly positive B_z which implies that the lobe reconnection voltage increasingly often exceeds the sum of ($\Phi_N + \Phi_V$).

In the ECPC model the spread at a given IMF B_z is expected because in non-steady state both Φ_D and Φ_N contribute to Φ_{PC}. From long-term averages (for which $\Phi_D = \Phi_{PC}$) we know that Φ_D varies approximately linearly with $-B_z$ for $B_z < 0$. It is also known that the auroral electrojet indices AE and AL vary approximately linearly with Φ_{PC}, again with considerable scatter (*Weimer et al*., 1990). In this paper we investigate the nightside auroral electrojet index AL as a proxy for the nightside voltage, Φ_N, which is consistent with its use as a substorm expansion phase identifier in substorm cycles. *Lockwood et al.* (2009) used satellite passes to show that statistically polar cap flux decayed (i.e., Φ_N is enhanced) during substorm expansion phases when $-AL$ is enhanced. *Hubert et al*. (2006) and *Milan et al*. (2009) used auroral images to also infer the loss of open flux during substorm expansion phases which also implies a relationship between $-AL$ and Φ_N. The variation of Φ_N inferred from time-constants by *Laundal* (2020) shows a strong variation with $-AL$ as does the analysis of the polar cap boundary location by *Aikio et al.* (2013).

Figure 7a plots the variation of the occurrence of combinations of the AL index and IMF B_z using the same bins in B_z as used in Figure 6 and bins of AL that are 10nT wide. The behaviour is quite similar to that for Φ_{PC} shown in Figure 6. Figure 7b shows the mean Φ_{PC} in the same bins as used in Figure 7a. Note that at constant AL, Φ_{PC} increases with increasingly negative B_z (moving horizontally to the left of the plot) but importantly, Φ_{PC} also increases with increasingly negative AL at constant B_z for $B_z < 0$ (moving vertically up the left-hand half of the plot). Hence Φ_{PC} increases with increases in both IMF $-B_z$ and $-AL$. Figure 8 color-codes the mean $-AL$ value in the same bins as used in Figure 6. It can be seen

that the spread in Φ_{PC} at a constant B_z is indeed associated with the spread in AL , as predicted by the ECPC model.

3-iii. Evolution of Φ_{PC} during northward IMF with time since the IMF turned northward

A second scatter plot that was important verification of the ECPC model was presented in Figure 6 of Wygant et al. (1983). The plot looked at Φ_{PC}values during northward IMF, as a function of time since the IMF last had a southward component. Shortly after a northward turning, *Wygant et al.* found almost the same range in Φ_{PC} as seen during southward IMF but largest observed Φ_{PC} declined exponentially with time the longer the period of northward IMF continued, until after 10 hours only low values were seen. This was explained by the ECPC model which predicted that the larger values were because there was a large Φ_N (despite Φ_D being small because the IMF was northward). Large Φ_N can still present because of the large open flux that had been produced in the growth phase prior to the northward turning of the IMF and that flux took time to be fully appended to the near-tail tail lobes by the solar wind flow. As the IMF remained northward the events of higher Φ_N depleted the open flux and so the maximum of subsequent events was reduced.

The *Wygant et al*. plot contained only 28 datapoints, it is here reproduced in Figure 9 for the 29373 datapoints available from our survey for IMF $B_z > 0$ and $n_e > 255$. To evaluate the time since the IMF had a southward component, we here use 6-minute box-car running means of IMF B_z to avoid periods of northward IMF being interrupted by just a brief interval of southward IMF. For each northward-IMF Φ_{PC} value observed at time t_o we evaluate the time at which the IMF turned northward in these 6-minute running means, t_n, and hence $\Delta t = t_o - t_n$. We did also try using running means over 15 minutes and 60 minutes and Figure 9 was not substantially changed other than the appropriate resolution in Δt was lowered. Again, because of the large number of samples, we colour code the fraction of samples $n/\Sigma n$ (on a logarithmic scale) in bins and Figure 9 uses bins in Φ_{PC} that are 2kV wide (as in Figures 6 and 8) and in Δt that are 6 min wide. The near-exponential decay of the largest Φ_{PC} found by *Wygant et al*. is clear in Figure 9 and the time constant for that decay is very similar in Figure 9, with Φ_{PC} reduced to almost constant value by $\Delta t = 15\ hrs$. The ECPC model predicts that the larger Φ_{PC} values at a given Δt will be due to larger Φ_N and hence greater $-AL$. Figure 10 confirms that this is indeed the case by plotting the mean of $-AL$ in the same bins

as used in Figure 9. . *Wilder et al.* (2008) have used SuperDARN data to show that the lobe reconnection voltage in the ionosphere saturates at about 15-20 kV and so the voltages shown in Figures 9 and 10 for Δt greater than about 15 hours after the IMF turned northward are consistent with the effects of lobe reconnection but the values above 20 kV at Δt below about 10 hours (when AL is also enhanced) are not.

3-iv. Effect of solar wind dynamic pressure, p_{SW}

In this section we investigate the effect of solar wind dynamic pressure p_{SW} on the tail of the magnetosphere. From Figure 5, we use p_{SW} values taken $\delta t = 75\ min$ before the corresponding AL and Φ_{PC} observation to allow for a propagation lag δt through the magnetosheath from the nose of the magnetosphere to sufficient distances down the tail to squeeze the tail reconnection site and so modulate the tail reconnection voltage Φ_N . The analysis was also carried out for $\delta t = 5\ min$ appropriate for the propagation from the nose of the magnetosphere to the dayside magnetopause and $\delta t = 120\ min$ that gives the peak correlation between p_{SW} and Φ_{PC}. The autocorrelation function of p_{SW} only falls to 0.5 at a lag of 6 hours and because of this great persistence in the p_{SW} data series, essentially the same features as shown here were observed for all three δt values used.

Figure 11 looks at the dependence on IMF B_z and the solar wind dynamic pressure (normalised by the mean, i.e. $p_{SW}/< p_{SW} >$) of (a) the mid-latitude am geomagnetic range index, (b) the mean $-AL$ and (c) the mean transpolar voltage Φ_{PC}. In all 3 panels means are given in bins are $\Delta B_z = 0.5nT$ wide in IMF B_z and 0.1 wide in $p_{SW}/< p_{SW} >$. The am index shows clear increases with increasing p_{SW} at all IMF B_z and, combined with the effect of B_z, this gives contours of constant mean am that are inclined to the vertical. This effect of p_{SW} on am has recently been identified and modelled by *Lockwood et al.* (2020a; b; 2021) as being the effect of p_{SW} on the near-Earth tail. The same variation is seen in both AL and Φ_{PC}; however, it is not as marked as for am and is much stronger for $B_z < 0$ than for $B_z > 0$. We infer AL and Φ_{PC} respond to increased Φ_N caused by the squeezing effect of p_{SW} on the magnetic shear across near-Earth cross tail current sheet whereas am also responds to the enhanced energy density stored in the tail lobes because of the same squeezing effect of p_{SW}. Figure 12 confirms the trends to higher values by showing the mean values, averaged over all IMF B_z, (with error bars of plus and minus 1 standard deviation that are large because of the

large variation introduced by B_z). The upward trend is seen in all three parameters but noticeably the gradient of the polynomial fit decreases at larger p_{SW} for both AL and Φ_{PC}.

Figure 13 shows that the p_{SW} effect does play a role in the behavour during northward IMF. This plot is the same as Figure 10 but shows the mean values of p_{SW} in the bins. It can be seen that the larger values of Φ_{PC} at a given time since the IMF turned northward tend to be at larger p_{SW}.

3-v. A sensitivity study of the effects of the availability of radar echoes

In the above sub-sections all the plots shown are for the number of radar echoes $n_e > n_{min} = 255$. All plots have also been generated using the 9 n_{min} $values$ given by the coloured lines in Figure 3. The trends in all plots are the same, the main effect being to change the absolute values in the means of Φ_{PC}. Figures 14 and 15 compare the variations of Φ_{PC} with IMF B_Z for the thresholds n_{min} of [100:100:900] with that for $n_{min} = 255$. In Figure 14 is for $n_{min} = 255$ and the mean values and standard deviations are given for each B_Z bin as well as the 6th-order polynomial fit (solid line). In figure 15 only the polynomial fits are plotted to avoid overplotting the multiple cases. It can be seen that the same behaviour is seen at all n_{min} values, the main difference being that Φ_{PC}values are systematically higher for larger n_{min} at all values of IMF B_Z. This is expected because removal of values based on low numbers of echoes systematically removes low Φ_{PC} samples, as shown by Figure 4. We note that this effect is seen for both northward and southward IMF samples, except for the very largest (positive) B_Z when the mean Φ_{PC} is close to 25kV, irrespective of the n_{min} used.

Figures 16 and 17 make the equivalent comparisons of the average variations of Φ_{PC} for $B_Z > 0$with time elapsed Δt since the IMF turned northward. Again the clear trend is to larger Φ_{PC} at larger n_{min}. However, this is not true at all Δt as the effect declines in amplitude at $\Delta t > 5hrs$ and is not seen at all at $\Delta t > 10hrs$, such that at the largest all n_{min} thresholds give a near constant Φ_{PC} of 15kV.

All the plots presented in the Sections 3-ii, 3-iii and 3-iv have been generated using all 9 n_{min} thresholds of n_e used in Figures 3, 4, 15 and 17. In every case the form of the plot is essentially the same, the main effect being that there are fewer samples available and so the plots cover smaller ranges of the parameters as noise due to lack of samples becomes a greater issue in the tails of the distributions.

4. Discussion and conclusions

4-i. The dependence of transpolar voltage on magnetic reconnection in both the magnetopause and the cross-tail current sheet

We have regenerated some of the scatter plots that formed an important basis for our understanding of magnetospheric and ionospheric convection. Those plots were generated using typically less than 100 satellite passes whereas we here increase those numbers by factors of about 1000 using convection patterns derived from the SuperDARN array of ground-based coherent radars.

In particular, we have reproduced plots of the variation of transpolar voltage Φ_{PC} with IMF B_z (e.g. *Cowley*, 1984) and the plot of Φ_{PC} for $B_z > 0$ with time elapsed since the IMF turned northward (*Wygant et al.*, 1983). We have used the *AL* auroral electrojet index to show that the scatter in these plots is well explained by the effect of the nightside voltage caused by reconnection in the cross-tail current sheet in Expanding-Contracting Polar Cap (ECPC) model, as was postulated in discussion of the model but has not been illustrated as clearly before now.

4-ii. Estimates of voltage due to viscous-like interaction across the magnetopause

We have demonstrated that the residual transpolar voltage after a period of southward IMF decays away with time elapsed since the IMF has been northward. After about 24 hours the voltage has decayed to $\Phi_{PC} \approx 15 kV$ and although in general Φ_{PC} values are slightly sensitive to our choice of how many echoes are required (n_{min}) to yield a valid Φ_{PC} estimate, we have shown that this is not true for this estimate of the residual Φ_{PC} after long (~1 day) intervals of northward IMF. There are some points that should be noted about this value. From the above discussion, if both Φ_N or Φ_D could be considered to be zero at these times then we get a maximum estimate of the viscously-like voltage $\Phi_V < \Phi_{PC} \approx 15\ kV$. This is maximum because our definition of Φ_{PC} means that lobe reconnection would set the value of Φ_{PC} if present and its effect in the ionosphere exceeded Φ_V.

Viscously-driven flows, by definition, appear in the region of closed field lines on the flank of the magnetosphere called the low-latitude boundary layer (LLBL, see Figure 1). One problem is defining what are closed field lines and *Fuselier et al.* (1999) have pointed out that some of the particle flux signatures traditionally used to identify closed field lines are actually best

explained as open field lines. *Mozer* (1984) surveyed 24 LLBL crossings and found the voltage across the LLBL on one flank ranged between 0 and 16 kV, with an average of 3 kV. *Mozer et al.* (1994) surveyed 41 such crossings and found an average value of 4 kV. If such a voltage existed on both flanks simultaneously this implies a viscous voltage Φ_V in the range 0-32kV with a mean value of 6kV. These values are obtained by integrating the along-track electric field seen by magnetospheric spacecraft as they pass through the LLBL. *Hapgood and Lockwood* (1993) pointed out that an assumption in these measurements is that the LLBL is stationary and that the satellite moves through it so that the LLBL thickness is the speed of the satellite times the time it resides in the LLBL. However, in general a better approximation would be that the satellite be considered still and the boundary moves over it and that large estimates in LLBL thickness and Φ_V can arise from a boundary that happens to be moving with the craft. They used plasma characteristics in the LLBL to show that for some cases of apparently large Φ_V the true value was, in fact, only about 3 kV.

Detailed study of convection reversals in the ionosphere near dawn and dusk indicates that sometimes the plasma motion across them exceeds the motion of the boundary, implying they are not just moving adiaroic boundaries and there is a genuinely viscous-like process at work (*Lockwood et al*, 1988; *Chen and Heelis*, 2018); however, in such cases the true boundary motion is very difficult to determine accurately and uncertainties are large making accurate determination of Φ_V by integrating along the boundary impossible. *Newell et al.* (1991) and *Sundberg et al.* (2008) used LEO observations of electric fields and particle precipitations to infer the voltage across the low-altitude footprint of the LLBL and find values manly below 10 kV with a few values over 20kV. There are two problems with this which may explain the larger values. Firstly, the identification of closed LLBL field lines from the particle precipitations is not definitive. Secondly, the ECPC model predicts that antisunward flow on closed field lines in the ionospheric projection of the LLBL can be generated by nightside reconnection and polar cap contraction because the convection reversal boundary can be shifted from the open-closed field line boundary by the conductivity distribution in the ionosphere.

From the above the estimate of $\Phi_V \leq 15\ kV$ derived from Figure 17 is somewhat higher than we would expect for an average value from a statistical survey. However, we stress here that this is a maximum value for Φ_V because it is derived assuming $\Phi_D = 0$ and $\Phi_N = 0$ with

lobe reconnection voltages lower than Φ_V. There are reasons to believe none of these assumptions is valid. Firstly, it has been shown from outward fluxes of ionospheric ion species that opening of field lines continues between the magnetic cusps at a low level even when the IMF points northward (*Chandler et al.*, 1999; *Fuselier et al*., 2000) and observations of simultaneous "double" cusps have been interpreted as subsolar reconnection continuing even though the IMF is northward and lobe reconnection is simultaneously taking place (*Lockwood and Moen*, 1999; *Pitout et al.*, 2002; *Lockwood et al.*, 2003). Hence although Φ_D is small during northward IMF it may be larger than zero. Secondly, as pointed out by *Lockwood* (2019), the tail lobes have never been seen to vanish, no matter how long the IMF remains northward. This means there is always a cross-tail current sheet with magnetic shear across it at which we would expect nightside reconnection to occur, even if the resulting Φ_N is small. Thirdly *Wilder et al.* (2008) use SuperDARN data to show that the lobe reconnection voltages in the ionosphere saturates at about 15-20 kV and hence the voltages seen at large times since the IMF turned northward are likely to be caused by lobe reconnection than by viscous-like interaction. As a consequence, the assumptions are all unlikely to be valid and we must treat 15kV as an upper limit to the average value of Φ_V and it is very likely to be lower than this.

4-iii. The effect of dynamic pressure

There are physical reasons to expect both the Φ_D and Φ_N to be increased by increased solar wind dynamic pressure p_{SW}. In both cases the compression brought about by greater p_{SW} should increase the magnetic shear across the current sheet and so enhance the reconnection rate. One caveat on this is that the nightside reconnection must be taking place at a GSM X-coordinate at which the tail is still flaring (i.e. the radius increases with increasingly negative X) and so the dynamic pressure can squeeze the tail lobe and so increase the lobe field and the cross tail current (*Caan et al*., 1973).

Using the *am* geomagnetic index as a proxy indicator of magnetopause reconnection, *Scurry and Russell* (1991) inferred statistically that dayside reconnection voltage Φ_D was indeed enhanced by increased p_{SW}. However much of the evidence for such an effect comes from transient responses to individual events in which p_{SW} increases suddenly (e.g., *Boudouridis et al*., 2003). The problem with these events is there will be a number of transient responses and of which the effect of p_{SW} on Φ_D is just one and isolating just that one effect is difficult.

An important effect of p_{SW} on the tail was demonstrated directly by *Karlsson et al.* (2000) who showed that near-Earth tail energy content was reduced if p_{SW} decreased and that such sudden decreases caused quenching of any substorm expansion that had recently begun. This strongly suggests reduced p_{SW} can reduce the nightside voltage, Φ_N. Conversely, increases in p_{SW} have been seen to trigger onsets of full substorm expansion phases (*Schieldge and Siscoe*, 1970; *Kokubun et al.*, 1977; *Yue et al.*, 2010) and have been identified as a cause of a rise in Φ_N (*Boudouridis et al*., 2008b). In some cases, the rise in Φ_N has been inferred from a loss of open flux as aurora expands into what appears to be open flux (*Hubert et al*., 2006a).

Various observational studies suggest that increases in p_{SW} cause enhanced general magnetospheric convection and field-aligned current systems as well as enhanced geomagnetic activity (e.g., *Lukianova*, 2003; *Lee et al*., 2004; *Hubert et al*., 2006b, *Boudouridis et al*., 2008a, *Stauning & Troshichev*, 2008). This phenomenon, has been modelled using global MHD models of the magnetosphere as being caused by rises in both Φ_D *and* Φ_N (*Palmroth et al*., 2004; *Ober et al.*, 2006; *Connor et al.*, 2014; *Lockwood et al.*, 2020b).

Figure 18 looks at the implications for any influence of p_{SW} on Φ_D and Φ_N of the correlations between p_{SW} and the auroral electrojet indices for both northward and southward IMF. It also compares the correlograms with those for p_{SW} and Φ_{PC} for northward and southward IMF that were shown in Figure 5. The blue and orange and lines are for AU and AL, respectively, for southward IMF ($B_Z < 0$). Both show a rapid response, although the correlation does not decay away for large positive lags as quickly for AL as it does for AU. Note that correlations are lower for the southward IMF data than for northward IMF (shown by the mauve and green lines) because the controlling influence of IMF B_Z is much greater in these cases. The mauve and green lines are for AU and AL, respectively and for northward IMF we see that AL responds to p_{SW} after a long lag, consistent with the squeezing of the tail by increased p_{SW} increasing Φ_N. From the peak correlation this appears to be a relatively weak effect compared to the peaks for AU: however, it must be remembered that the lag for the dayside effect is short and much less variable than for any effect on the nightside and so we should expect a broad, but relatively low, peak for the effect on AL. Note also the peak for AU at short lags for northward IMF implies that the dayside reconnection is not only enhanced by increased p_{SW} when the IMF is southward, but that it may still present and enhanced by

p_{SW} when it is IMF is northward. *Finch et al.* (2008) and *Lockwood et al.* (2020a) found that the effect of p_{SW} on mid-latitude range indices was via the nightside substorm current wedge and associated with Φ_N and was the origin of the equinoctial time-of-day/time-of-year pattern of geomagnetic activity via the effect of the dipole tilt. The modelling analysis of *Lockwood et al.* (2020b) found both influence of p_{SW} via both Φ_N and the energy stored in the tail lobe. The results presented here show an effect of p_{SW} on Φ_{PC}, but that the effect of is smaller than for am: this indicates that the effect of energy stored in the tail is a larger factor for mid-latitude range indices such as am .

As mentioned above, the studies of transient responses do not necessarily reveal the dependence of Φ_D *and* Φ_N , and hence Φ_{PC}, on p_{SW} because of other transient responses although they do imply a connection. We here have shown that there is a connection on a statistical basis. One potential problem is that p_{SW} has many parameters in common with the power input into the magnetosphere, but *Lockwood et al.* (2020a; b, 2021) have demonstrated that it has a separate and distinct influence on the am mid-latitude, range geomagnetic activity index. We here have demonstrated that p_{SW} has a similar influence on the nightside auroral AL index and the transpolar voltage Φ_{PC}.

Acknowledgements. This work is supported by a number of grants. ML is supported by STFC consolidated grant number ST/M000885/1 and by the SWIGS NERC Directed Highlight Topic Grant number NE/P016928/1/. Funding for KAM at University of Saskatchewan was provided by the Canadian Foundation for Innovation (CFI), the Province of Saskatchewan, and a Discovery Grant from the Natural Sciences and Engineering Research Council (NSERC) of Canada. Initial work by KAM for this paper was carried out at University of Reading on sabbatical leave from University of Saskatchewan. The authors acknowledge the use of SuperDARN data. SuperDARN is a collection of radars funded by national scientific funding agencies of Australia, Canada, China, France, Japan, South Africa, United Kingdom and United States of America. The authors are also grateful to the staff of: the Space Physics Data Facility, NASA/Goddard Space Flight Center, who prepared and made available the OMNI2 dataset used: these interplanetary data were downloaded from http://omniweb.gsfc.nasa.gov/ow.html; the World Data Center for Geomagnetism, Kyoto who generate and make available the *AL* index from http://wdc.kugi.kyoto-u.ac.jp/aeasy/index.html and the staff of L'École et Observatoire des Sciences de la Terre

(EOST), a joint of the University of Strasbourg and the French National Center for Scientific Research (CNRS) and the International Service of Geomagnetic Indices (ISGI) for making the am index data available from http://isgi.unistra.fr/data_download.php

References

Aikio, A., Pitkänen, T., Honkonen, I., Palmroth, M., Amm, O. (2013) IMF effect on the polar cap contraction and expansion during a period of substorms, *Annales Geophysicae*, **31**: 1021-1034 , doi: 10.5194/angeo-31-1021-2013

Baker, D. N., Klimas, A. J., Vassiliadis, D., Pulkkinen, T. I., and McPherron, R. L. (1997), Reexamination of driven and unloading aspects of magnetospheric substorms, J. *Geophys. Res.*, 102 (A4), 7169– 7177, doi: 10.1029/96JA02627.

Baker, D. N., Zwickl, R. D., Bame, S. J., Hones, E. W., Tsurutani, B. T., Smith, E. J., and Akasofu, S.-I. (1983), An ISEE 3 high time resolution study of interplanetary parameter correlations with magnetospheric activity, *J. Geophys. Res*., **88** (A8), 6230– 6242, doi:10.1029/JA088iA08p06230.

Boudouridis, A., L.R. Lyons, E. Zesta, and J. M. Ruohoniemi (2007), Dayside reconnection enhancement resulting from a solar wind dynamic pressure increase, *J. Geophys. Res*., **112**, A06201, doi:10.1029/2006JA012141.

Boudouridis, A., E. Zesta, L. R. Lyons, P. C. Anderson, and A. J. Ridley (2008a), Temporal evolution of the transpolar potential after a sharp enhancement in solar wind dynamic pressure, *Geophys. Res. Lett*., **35**, L02101, doi:10.1029/2007GL031766.

Boudouridis, A., L. R. Lyons, E. Zesta, J. M. Ruohoniemi, and D. Lummerzheim (2008b), Nightside flow enhancement associated with solar wind dynamic pressure driven reconnection, *J. Geophys. Res*., **113**, A12211, doi:10.1029/2008JA013489.

Boyle, C. B., Reiff, P. H., and Hairston, M. R. (1997), Empirical polar cap potentials, *J. Geophys. Res*., **102** (A1), 111– 125, doi:10.1029/96JA01742.

Bristow, W. A., R. A. Greenwald, S. G. Shepherd, and J. M. Hughes (2004), On the observed variability of the cross–polar cap potential, *J. Geophys. Res*., **109**, A02203, doi: 10.1029/2003JA010206.

Caan M.N., McPherron R.L., Russell C.T. (1973), Solar wind and substorm-related changes in the lobes of the geomagnetic tail. *J. Geophys. Res.*,**78** (34): 8087–8096. doi: 10.1029/ja078i034p08087.

Chandler, M.O., S.A. Fuselier, M. Lockwood and T.E. Moore (1999), Evidence of component magnetic merging equatorward of the cusp, *J. Geophys. Res*., **104** , 22623-22648, doi: 10.1029/1999JA900175.

Chen, Y.-J., & Heelis, R. A. (2018). Motions of the convection reversal boundary and local plasma in the high-latitude ionosphere, *Journal of Geophysical Research: Space Physics*,**123**, 2953–2963. doi: 10.1002/2017JA024934

Chisham, G., Lester, M., Milan, S. E., Freeman, M. P., Bristow, W. A., Grocott, A., McWilliams, K. A., Ruohoniemi, J. M., Yeoman, T. K., Dyson, P. L., Greenwald, R. A., Kikuchi, T., Pinnock, M., Rash, J. P. S., Sato, N., Sofko, G.J., Villain, J.-P., Walker, A. D. M. (2007), A decade of the Super Dual Auroral Radar Network (SuperDARN): scientific achievements, new techniques and future directions, *Surveys in Geophys*., **28** (1), 33-109, doi: 10.1007/s10712-007-9017-8.

Connor, H. K., E. Zesta, D. M. Ober, and J. Raeder (2014), The relation between transpolar potential and reconnection rates during sudden enhancement of solar wind dynamic pressure: OpenGGCM-CTIM results, *J. Geophys. Res. Space Physics*, **119**, 3411–3429, doi: 10.1002/2013JA019728.

Consolini, G., and De Michelis, P. (2005), Local intermittency measure analysis of AE index: The directly driven and unloading component, *Geophys. Res. Lett.*, **32**, L05101, doi:10.1029/2004GL022063.

Cousins, E. D. P., Matsuo, T., and Richmond, A. D. (2013), SuperDARN assimilative mapping, *J. Geophys. Res. Space Physics*, **118**, 7954– 7962, doi:10.1002/2013JA019321.

Cowley, S. W. H. (1982), The causes of convection in the Earth's magnetosphere: A review of developments during the IMS, *Rev. Geophys*., **20** (3), 531– 565, doi:10.1029/RG020i003p00531.

Cowley, S.W.H. (1984), Solar wind control of magnetospheric convection. *Achievements of the International Magnetospheric Study (IMS)*, Proceedings of an International Symposium, Graz, Austria, 26-28 June 1984, **ESA-SP-*217***, Eds. B. Battrick and E.J. Rolfe., p.483, European Space Agency. ISSN 0379-6566

Cowley, S. W. H., and Lockwood, M. (1992), Excitation and decay of solar-wind driven flows in the magnetosphere-ionosphere system, *Annales Geophys*., **10**, 103-115.

Cowley, S.W.H., Freeman, M.P., Lockwood, M. and Smith, M.F. (1991) The ionospheric signature of flux transfer events, in "*CLUSTER - dayside polar cusp*", ed. C.I. Barron, ESA SP-330, 105-112, European Space Agency Publications, Nordvijk, The Netherlands

Davis, T. N., and Sugiura, M. (1966), Auroral electrojet activity index AE and its universal time variations, *J. Geophys. Res.*, **71** (3), 785–801, doi:10.1029/JZ071i003p00785.

DeJong, A. D., Ridley, A. J., and Clauer, C. R. (2008), Balanced reconnection intervals: four case studies, *Ann. Geophys*., **26**, 3897–3912, doi: 10.5194/angeo-26-3897-2008, 2008.

Drayton, R. A., Koustov, A. V., Hairston, M. R., and Villain, J.-P. (2005), Comparison of DMSP cross-track ion-drifts and SuperDARN line-of-sight velocities, *Annales Geophysicae*, **23** (7), 2479–2486, doi: 10.5194/angeo-23-2479-2005.

Echer, E., Korth, A., Bolzan, M. J. A., & Friedel, R. H. W. (2017), Global geomagnetic responses to the IMF B_z fluctuations during the September/October 2003 high-speed stream intervals, *Annales Geophys*., **35** (4), 853-868, doi: 10.5194/angeo-35-853-2017.

Etemadi, A., Cowley, S. W. H., Lockwood, M. , Bromage, B. J. I., Willis, D. M. and Lühr, H. (1988), The dependence of high-latitude dayside ionospheric flows on the north-south component of the IMF: a high time resolution correlation analysis using EISCAT "POLAR" and AMPTE UKS and IRM data, *Planet. Space Sci.*, **36**, 471-498, doi: 10.1016/0032-0633(88)90107-9.

Farrugia, C.J., Gratton, F.T. & Torbert, R.B (2001), Viscous-type processes in the solar wind-magnetosphere interaction. *Space Science Reviews* 95, 443–456. doi: 10.1023/A:1005288703357

Finch, I. D., Lockwood, M., and Rouillard, A. P. (2008), The effects of solar wind magnetosphere coupling recorded at different geomagnetic latitudes: separation of directly-driven and storage/release systems, *Geophys. Res. Lett*., **35**, L21105, doi:10.1029/2008GL035399.

Fuselier, S.A., M. Lockwood, T.G. Onsager and W.K. Peterson (1999) The source population for the cusp and cleft/LLBL for southward IMF, *Geophys. Res. Lett*., **26**, 1665-1669, doi: 10.1029/1999GL900354.

Fuselier, S.A., Trattner, K. J., and Petrinec, S. M. (2000), Cusp observations of high- and low-latitude reconnection for northward interplanetary magnetic field, *J. Geophys. Res*., **105** (A1), 253– 266, doi:10.1029/1999JA900422.

Greenwald, R. A., Bristow, W. A., Sofko, G. J., Senior, C., Ceriser, J.-C., and Szabo, A. (1995), Super Dual Auroral Radar Network radar imaging of dayside high-latitude convection under northward interplanetary magnetic field: toward resolving the distorted two-cell versus multicell controversy, *J. Geophys. Res.*, **100**, 19661–19674, doi: 10.1029/95ja01215.

Gao, Y. (2012), Comparing the cross polar cap potentials measured by SuperDARN and AMIE during saturation intervals, *J. Geophys. Res*., **117**, A08325, doi: 10.1029/2012JA017690.

Gordeev, E. I., Sergeev, V. A., Pulkkinen, T. I., and Palmroth, M. (2011), Contribution of magnetotail reconnection to the cross-polar cap electric potential drop, *J. Geophys. Res.*, **116**, A08219, doi:10.1029/2011JA016609.

Haines, C. A., Owens, M. J., Barnard, L. A., Lockwood, M., and Ruffenach, A. (2019) The variation of geomagnetic storm duration with intensity, *Solar Physics*, **294**, 154, pp1-15, doi: 10.1007/s11207-019-1546-z.

Hairston, M. R., Heelis, R. A., and Rich, F. J. (1998), Analysis of the ionospheric cross polar cap potential drop using DMSP data during the National Space Weather Program study period, *J. Geophys. Res.*, **103** (A11), 26337– 26347, doi: 10.1029/97JA03241.

Hanson, W. B., Coley, W. R., Heelis, R. A., Maynard, N. C., and Aggson, T. L. (1993), A Comparison of in situ measurements of $\vec{E}$ and $-\vec{V}\times\vec{B}$ from Dynamics Explorer 2, *J. Geophys. Res.*, **98** (A12), 21501– 21516, doi:10.1029/93JA01422.

Hapgood, M.A., and M. Lockwood (1993) On the voltage and distance across the low-latitude boundary layer, *Geophys. Res. Lett*., **20**, 145-148, doi: 10.1029/93GL00063

Hapgood, M. A., Bowe, G., Lockwood, M., Willis, D. M., and Tulunay, Y. (1991) Variability of the interplanetary magnetic field at 1 A.U. over 24 years: 1963 – 1986, *Planet. Space Sci.*, **39**, 411-423, doi: 10.1016/0032-0633(91)90003-S.

Holzer, R. E., McPherron, R. L., and Hardy, D. A. (1986), A quantitative empirical model of the magnetospheric flux transfer process, *J. Geophys. Res*., **91**(A3), 3287– 3293, doi:10.1029/JA091iA03p03287.

Huang, C.-S., A. D. DeJong, and X. Cai (2009), Magnetic flux in the magnetotail and polar cap during sawteeth, isolated substorms, and steady magnetospheric convection events, *J. Geophys. Res*., **114**, A07202, doi: 10.1029/2009JA014232.

Hubert, B., M. Palmroth, T. V. Laitinen, P. Janhunen, S. E. Milan, A. Grocott, S. W. H. Cowley, T. Pulkkinen, and J.-C. Gérard (2006a), Compression of the Earth's magnetotail by interplanetary shocks directly drives transient magnetic flux closure, *Geophys. Res. Lett*., **33**, L10105, doi:10.1029/2006GL026008

Hubert, B., Milan, S. E., Grocott, A., Blockx, C., Cowley, S. W. H., and Gérard, J.-C. (2006b), Dayside and nightside reconnection rates inferred from IMAGE FUV and Super Dual Auroral Radar Network data, *J. Geophys. Res*., **111**, A03217, doi:10.1029/2005JA011140

Imber, S. M., Milan, S. E., and Lester, M. (2013) Solar cycle variations in polar cap area measured by the superDARN radars, *Journal of Geophysical Research: Space Physics*, **118** (10), 6188 – 6196, doi: 10.1002/jgra.50509.

Karlsson, S.B.P., Opgenoorth, H.J., Eglitis, P., Kauristie, K, Syrjäsuo, M., Pulkkinen, T.I., Lockwood, M., Nakamura, R., Reeves, G., Romanov, S. (2000) Solar wind control of magnetospheric energy content: substorm quenching and multiple onsets. *J. Geophys. Res*., **105**, 5335-5356, doi: 10.1029/1999JA900297

Kokubun S. McPherron, R.L. Russell, C.T. (1977) Triggering of substorms by solar wind discontinuities. *J. Geophys. Res*., **82** (1) 74-86, doi: 10.1029/ja082i001p00074.

Klimas, A. J., Baker, D. N., Vassiliadis, D., and Roberts, D. A. (1994), Substorm recurrence during steady and variable solar wind driving: *Evidence* for a normal mode in the unloading dynamics of the magnetosphere, *J. Geophys. Res*., **99**, 14855–14861. doi: 10.1029/94JA01240.

Koustov, A. V., Lavoie, D. B., Kouznetsov, A. F., Burchill, J. K., Knudsen, D. J., & Fiori, R. A. D. (2019a), A comparison of cross-track ion drift measured by the Swarm satellites and plasma convection velocity measured by SuperDARN, *Journal of Geophysical Research: Space Physics*,**124**, 4710–4724, doi: 10.1029/2018JA026245

Koustov, A. V., Ullrich, S., Ponomarenko, P. V., Nishitani, N., Marcucci, F. M., Bristow, W. A. (2019b), Occurrence of F region echoes for the polar cap SuperDARN radars, *Earth Planets Space*, **71**, 112 (2019b). doi: 10.1186/s40623-019-1092-9

Kubota, Y., Nagatsuma, T., Den, M., Tanaka, T., and Fujita, S. (2017), Polar cap potential saturation during the Bastille Day storm event using global MHD simulation, *J. Geophys. Res. Space Physics*, **122**, 4398–4409, doi:10.1002/2016JA023851.

Laundal, K.M., Reistad, J.P., Hatch, S.M. et al. (2020) Time-scale dependence of solar wind-based regression models of ionospheric electrodynamics. *Sci. Rep.* **10**, 16406. doi: 10.1038/s41598-020-73532-z

Lee D.-Y., Lyons L.R., Yumoto K. (2004), Sawtooth oscillations directly driven by solar wind dynamic pressure enhancements, *J. Geophys. Res*., **109**, A04202. doi: 10.1029/2003JA010246.

Lockwood, M. (1991), On flow reversal boundaries and cross-cap potential in average models of high latitude convection, *Planet. Space Sci*., **39**, 397-409, doi: 10.1016/0032-0633(91)90002-R.

Lockwood, M. (2013) Reconstruction and Prediction of Variations in the Open Solar Magnetic Flux and Interplanetary Conditions, *Living Reviews in Solar Physics*, **10**, 4, 2013. doi: 10.12942/lrsp-2013-4

Lockwood, M. (2019), Does adding solar wind Poynting flux improve the optimum solar wind-magnetosphere coupling function? *J. Geophys. Res. (Space Physics)*, **124** (7), 5498-5515, doi: 10.1029/2019JA026639.

Lockwood, M., and Cowley, S.W.H. (1992) Ionospheric Convection and the substorm cycle in "Substorms 1, Proceedings of the First International Conference on Substorms, ICS-1", ed C. Mattock, ESA-SP-335, 99-109, European Space Agency Publications, Nordvijk, The Netherlands.

Lockwood, M., and Moen, J. (1999) Reconfiguration and closure of lobe flux by reconnection during northward IMF: evidence for signatures in cusp/cleft auroral emissions, *Annales Geophys*., **17**, 996-1011, doi: 10.1007/s00585-999-0996-2.

Lockwood, M., and Morley, S. E. (2004), A numerical model of the ionospheric signatures of time-varying magnetic reconnection: I. Ionospheric convection, *Annales Geophys*., **22**, 73-91, doi: 10.5194/angeo-22-73-2004.

Lockwood, M., van Eyken, A. P., Bromage, B. J. I., Willis, D. M., and Cowley, S. W. H. (1986), Eastward propagation of a plasma convection enhancement following a southward turning of the interplanetary magnetic field, *Geophys. Res. Lett*., **13**, 72-75, doi: 10.1029/GL013i001p00072.

Lockwood, M., S.W.H. Cowley, H. Todd, D.M. Willis and C.R. Clauer (1988) Ion flows and heating at a contracting polar cap boundary, *Planet. Space Sci.*, **36**, 1229-1253, doi: 10.1016/0032-0633(88)90076-1

Lockwood, M., Cowley, S. W. H., and Freeman, M. P. (1990), The excitation of plasma convection in the high latitude ionosphere, *J. geophys Res*., **95**, 7961-7971, doi: 10.1029/JA095iA06p07961, 1990

Lockwood, M., Denig, W.F., Farmer, A.D., Davda, V.N., Cowley, S.W.H and Lühr, H. (1993) Ionospheric signatures of pulsed magnetic reconnection at the Earth's magnetopause, *Nature*, **361** (6411), 424-428. doi: 10.1038/361424a0

Lockwood , M., B.S. Lanchester , H. Frey , K. Throp, S. Morley, S.E. Milan, and M.E. Lester (2003) IMF Control of Cusp Proton Emission Intensity and Dayside Convection: implications for component and anti-parallel reconnection, *Annales Geophys*., **21**, 955 982, doi: 10.5194/angeo-21-955-2003

Lockwood, M., Throp, K.. Lanchester, B. S., Morley, S. K., Milan, S. E., Lester, M., and H. U. Frey, H. U. (2006), Modelling the observed proton aurora and ionospheric convection responses to changes in the IMF field clock angle: 2. The persistence of ionospheric convection, *J. Geophys. Res*., **111**, A02306, doi:10.1029/2003JA010307.

Lockwood, M., Hairston, M. R., Finch, I. D., and Rouillard, A. P. (2009), Transpolar voltage and polar cap flux during the substorm cycle and steady convection events, *J. Geophys. Res.*, **114**, A01210, doi: 10.1029/2008JA013697.

Lockwood, M., Owens, M. J., Barnard, L. A., Bentley, S., Scott, C. J., and Watt, C. E. (2016), On the Origins and Timescales of Geoeffective IMF, *Space Weather*, **14**, 406 432, doi: 10.1002/2016SW001375.

Lockwood, M., Owens, M. J., Barnard, L. A., Scott, C. J., and Watt, C. E. (2017), Space Climate and Space Weather over the past 400 years: 1. The Power input to the Magnetosphere, *J. Space Weather Space Clim*., **7**, A25, doi: 10.1051/swsc/2017019.

Lockwood, M., Chambodut, A., Barnard, L. A., Owens, M. J., Clarke, E., and Mendel, V. (2018a), A homogeneous aa index: 1. Secular variation, *J. Space Weather Space Clim*., **8**, A53, doi: 10.1051/swsc/2018038.

Lockwood, M., Finch, I. D., Chambodut, A., Barnard, L. A., Owens, M. J., and Clarke, E. (2018b), A homogeneous aa index: 2. hemispheric asymmetries and the equinoctial variation, *J. Space Weather Space Clim*., **8**, A58, doi: 10.1051/swsc/2018044.

Lockwood, M., Bentley, S., Owens, M. J., Barnard, L. A., Scott, C. J., Watt, C. E. and Allanson, O. (2019a), The development of a space climatology: 1. Solar-wind magnetosphere coupling as a function of timescale and the effect of data gaps, *Space Weather*, 17, 133-156, doi: 10.1029/2018SW001856.

Lockwood, M., K.A. McWilliams, M.J. Owens, L.A. Barnard, C.E. Watt, C.J. Scott, A. McNeill and J.C. Coxon (2020a) Semi-annual, annual and Universal Time variations in the magnetosphere and in geomagnetic activity: 2. Response to solar wind power input and relationships with solar wind dynamic pressure and magnetospheric flux transport, *J. Space Weather Space Clim*., **10**, 30, doi: 10.1051/swsc/2020033

Lockwood, M., M.J. Owens, L.A. Barnard, C.E. Watt, C.J. Scott, J.C. Coxon and K.A. McWilliams (2020b) Semi-annual, annual and Universal Time variations in the magnetosphere and in geomagnetic activity: 3. Modelling, *J. Space Weather and Space Climate*, **10**, 61 doi: 10.1051/swsc/2020062

Lockwood, M., C.A. Haines, L.A. Barnard, J. Owens, C.J. Scott, A. Chambodut, and K.A. McWilliams (2021) Semi-annual, annual and Universal Time variations in the magnetosphere and in geomagnetic activity: 4. Polar Cap motions and origins of the Universal Time effect, *J. Space Weather and Space Climate*, **11**, 15, doi: 10.1051/swsc/2020077

Lopez, R. E., Wiltberger, M., Lyon, J. G., Goodrich, C. C., Papadopoulos, K. (1999) MHD simulations of the response of high-latitude potential patterns and polar cap boundaries to sudden southward turnings of the interplanetary magnetic field, *Geophys. Res. Lett*., **26** (7), 967 – 970, doi: 10.1029/1999GL900113.

Lopez, R. E., Lyon, J. G., Wiltberger, M. J., Goodrich, C. C. (2001) Comparison of global MHD simulation results with actual storm and substorm events, *Adv. Space Res*., **28**, (12), 1701-1706, doi: 10.1016/S0273-1177(01)00535-X

Lukianova R. (2003), Magnetospheric response to sudden changes in solar wind dynamic pressure inferred from polar cap index, *J. Geophys. Res*., **108**(A12), 1428 doi: 10.1029/2002JA009790.

Mayaud, P.-N. (1980), Derivation, Meaning and Use of Geomagnetic Indices, *Geophysical Monograph, 22*, American Geophysical Union, Washington, DC. doi: 10.1029/GM022.

McPherron, R. L. (2020), Early studies in solar wind coupling and substorms, *Journal of Geophysical Research: Space Physics*, 125, e2019JA027615, doi: 10.1029/2019JA027615.

McPherron, R.L., Baker, D. N., Bargatze, L. F., Clauer, C. R., and Holzer, R. E. (1998), IMF control of geomagnetic activity, *Adv. Space Res.*, **8** (9–10), 71-86, doi: 10.1016/0273-1177(88)90114-7.

McWilliams, K.A., Yeoman, T. K., and Cowley, S. W. H (2000) Two-dimensional electric field measurements in the ionospheric footprint of a flux transfer event, *Annales Geophys*., **18** (12), 1584 -1598. doi: 10.1007/s00585-001-1584-2

McWilliams, K. A., Pfeifer, J. B., and McPherron, R. L. (2008), Steady magnetospheric convection selection criteria: Implications of global SuperDARN convection measurements, *Geophys. Res. Lett*., **35**, L09102, doi:10.1029/2008GL033671.

Milan, S. E. (2004), Dayside and nightside contributions to the cross polar cap potential: placing an upper limit on a viscous-like interaction, *Ann. Geophys*., **22**, 3771–3777, doi: 10.5194/angeo-22-3771-2004.

Milan, S. E., Lester, M., Cowley, S. W. H. Oksavik, K., Brittnacher, M., Greenwald, R. A., Sofko, G., and Villain, J.-P. (2003), Variations in the polar cap area during two substorm cycles, *Annales Geophys*., **21** (5),1121-1140, doi: 10.5194/angeo-21-1121-2003.

962 Milan, S. E., Hutchinson, J., Boakes, P. D., and Hubert, B. (2009), Influences on the radius of
963 the auroral oval, *Annales Geophys*, **21** (5), 1121-1140. doi: 10.5194/angeo-21-1121-2003.

964 Milan, S. E., Gosling, J. S., and Hubert, B. (2012), Relationship between interplanetary
965 parameters and the magnetopause reconnection rate quantified from observations of the
966 expanding polar cap, *J. Geophys. Res*., **117**, A03226, doi: 10.1029/2011JA017082.

967 Milan, S. E., Carter, J. A., Sangha, H., Bower, G. E., & Anderson, B. J. (2021).
968 Magnetospheric flux throughput in the Dungey cycle: Identification of convection state during
969 2010. *Journal of Geophysical Research: Space Physics*, **126**, e2020JA028437. doi:
970 10.1029/2020JA028437

971 Mishin V. V. Karavaev Yu. A. (2017) Saturation of the magnetosphere during superstorms:
972 new results from the magnetogram inversion technique, *Solar-Terrestrial Physics*, **3** (3), 28-
973 36, doi: 10.12737/stp-33201704

974 Morley, S. E., and Lockwood, M. (2005), A numerical model of the ionospheric signatures of
975 time-varying magnetic reconnection: II. Measuring expansions in the ionospheric flow
976 response, *Annales Geophys.*, **23**, 2501-2510, doi: 10.5194/angeo-23-2501-2005

977 Mozer, F.S. (1984), Electric field evidence on the viscous interaction at the magnetopause.
978 *Geophys. Res. Lett.*, **11**, 135-138. doi: 10.1029/GL011i002p00135

979 Mozer, F.S., H. Hayakawa, S. Kokubun, M. Nakamura, T. Okada, T. Yamamoto and K.
980 Tsuruda (1994) The morningside low-latitude boundary layer as determined from electric and
981 magnetic field measurements on Geotail, *Geophys. Res. Lett.*, **21** (25), 2983-2986, doi:
982 10.1029/94GL01296

983 Newell, P. T., W. J. Burke, E. R. Sanchez, et al. (1991), The low-latitude boundary layer and
984 the boundary plasma sheet at low altitude: Prenoon precipitation regions and convection
985 reversal boundaries, *J. Geophys.Res*., 96, 21,013–21,023, doi: 10.1029/91ja01818

986 Nishida, A. (1968a), Coherence of geomagnetic DP 2 fluctuations with interplanetary
987 magnetic variations, *J. Geophys. Res.*, **73** (17), 5549– 5559, doi: 10.1029/JA073i017p05549.

988 Nishida, A. (1968b), Geomagnetic DP 2 fluctuations and associated magnetospheric
989 phenomena, *J. Geophys. Res*., **73** (5), 1795– 1803, doi: 10.1029/JA073i005p01795.

990 Ober, D. M., G. R. Wilson, N. C. Maynard, W. J. Burke, and K. D. Siebert (2006), MHD
991 simulation of the transpolar potential after a solar-wind density pulse, *Geophys. Res. Lett.*,
992 **539**(33), L04106, doi:10.1029/2005GL024655.

993 Palmroth, M., Pulkkinen, T.I., Janhunen, P., McComas, D.J., Smith, C.W., Koskinen, H.E.J.
994 (2004), Role of solar wind dynamic pressure in driving ionospheric Joule heating, *J. Geophys.*
995 *Res.*, **109**, A11302, doi: 10.1029/2004JA010529.

996 Pitout, F., Newell, P.T. and Buchert, S.C. (2002) Simultaneous high-and low-latitude
997 reconnection: ESR and DMSP observations, *Annales Geophys*., **20** (9), 1311-1320, doi:
998 10.5194/angeo-20-1311-2002

Provan, G., Yeoman, T. K., Milan, S. E., Ruohoniemi, J. M., and Barnes, R. (2002) An assessment of the ‘‘map-potential’’ and ‘‘beam-swinging’’ techniques for measuring the ionospheric convection pattern using data from the SuperDARN radars, *Annales Geophys*, **20**, 191–202, doi: 10.5194/angeo-20-191-2002.

Reiff, P. H., Spiro, R. W., and Hill, T. W. (1981), Dependence of polar cap potential drop on interplanetary parameters, *J. Geophys. Res*., **86** (A9), 7639– 7648, doi: 10.1029/JA086iA09p07639.

Ruohoniemi, J. M., and Baker K. B, (1998) Large-scale imaging of high-latitude convection with Super Dual Auroral Radar Network HF radar observations, *J. Geophys. Res.*, **103**, 20797–20811, doi: 10.1029/98ja01288.

Saunders, M. A., Freeman, M. P., Southwood, D. J., Cowley, S. W. H., Lockwood, M., Samson, J. C., Farrugia, C. J., and Hughes, T. J. (1992) Dayside ionospheric convection changes in response to long period IMF oscillations: determination of the ionospheric phase velocity, *J. Geophys. Res*., **97**, 19373-19380, doi: 10.1029/92JA01383.

Schieldge, J.P., Siscoe, G.L. (1970) A correlation of the occurrence of simultaneous sudden magnetospheric compressions and geomagnetic bay onsets with selected geophysical indices. *J. Atmos. Terr. Phys*., **32** (11), 1819-1830, doi: 10.1016/0021-9169(70)90139-x.

Scurry, L., and Russell, C. T. (1991), Proxy studies of energy transfer to the magnetosphere, *J. Geophys. Res*., **96** (A6), 9541– 9548, doi:10.1029/91JA00569.

Shepherd, S. G., and Ruohoniemi, J. M. (2000), Electrostatic potential patterns in the high-latitude ionosphere constrained by SuperDARN measurements, *J. Geophys. Res*., **105**, 23005–23014, doi: 10.1029/2000ja000171.

Siscoe, G. L., and Huang, T. S. (1985), Polar cap inflation and deflation, *J. Geophys. Res*., **90** (A1), 543– 547, doi:10.1029/JA090iA01p00543.

Stauning P., Troshichev, O.A. (2008), Polar cap convection and PC index during sudden changes in solar wind dynamic pressure, *J. Geophys. Res*., **113**, A08227, doi: 10.1029/2007JA012783.

Sundberg, K. Å. T., Blomberg, L. G., and Cumnock, J. A. (2008), Statistical analysis of the sources of the cross-polar potential for southward IMF, based on particle precipitation characteristics, *Geophys. Res. Lett*., **35**, L08103, doi:10.1029/2008GL033383

Throp, K., M. Lockwood, B. S. Lanchester, S. K. Morley, and H. U. Frey (2005) Modeling the observed proton aurora and ionospheric convection responses to changes in the IMF clock angle: 1. Persistence of cusp proton aurora, *J. Geophys. Res.*, **110**, A12311, doi: 10.1029/2003JA010306

Todd, H., Cowley, S. W. H., Etemadi, A., Bromage, B. J. I., Lockwood, M., Willis, D. M., and Lühr, H. (1988) Flow in the high-latitude ionosphere: measurements at 15-second resolution made using the EISCAT "POLAR" experiment, *J. atmos. terr. Phys.*, **50**, 423-446, doi: 10.1016/0021-9169(88)90026-8.

Weigel, R. S. (2007), Solar wind time history contribution to the day-of-year variation in geomagnetic activity, *J. Geophys. Res*., 112, A10207, doi:10.1029/2007JA012324.

Weimer, D. R., Maynard, N. C., Burke, W. J., & Liebrecht, C. (1990), Polar cap potentials and the auroral electrojet indices, *Planetary and space science*, **38**(9), 1207-1222. doi: 10.1016/0032-0633(90)90028-o

Wilder, F. D., Clauer, C. R., and Baker, J. B. H. (2008), Reverse convection potential saturation during northward IMF, *Geophys. Res. Lett*., **35**, L12103, doi:10.1029/2008GL034040.

Wilder, F. D., Clauer, C. R., Baker, J. B. H., Cousins, E. P., and Hairston, M. R. (2011) The nonlinear response of the polar cap potential under southward IMF: A statistical view, *J. Geophys. Res*., **116**, A12229, doi:10.1029/2011JA016924.

Wygant, J. R., Torbert, R. B., and Mozer, F. S. (1983), Comparison of S3-3 polar cap potential drops with the interplanetary magnetic field and models of magnetopause reconnection, *J. Geophys. Res*., **88** (A7), 5727– 5735, doi:10.1029/JA088iA07p05727.

Xu, L., Koustov, A. V. Xu, J. S., Drayton, R. A., and Huo, L. (2007a), A 2-D comparison of ionospheric convection derived from SuperDARN and DMSP measurements, *Adv. Space Res.,* **42** (7), 1259-1266, doi: 10.1016/j.asr.2007.06.044.

Xu, L., Xu, J., Alexandre, K., Papitashvili, V., and Rich, F. (2007b) A comparison of SuperDARN-derived plasma convection and DMSP ion drift measurements, *Wuhan Univ. J. of Nat. Sci*., **12**, 279–283. doi: 10.1007/s11859-006-0024-2

Yue, C., Zong, Q.G., Zhang, H., Wang, Y.F., Yuan, C.J., Pu, Z.Y., Fu, S.Y., Lui, A.T.Y., Yang, B., Wang, C.R. (2010), Geomagnetic activity triggered by interplanetary shocks. *J. Geophys. Res*. **115**, A00I05. doi: 10.1029/2010JA015356.

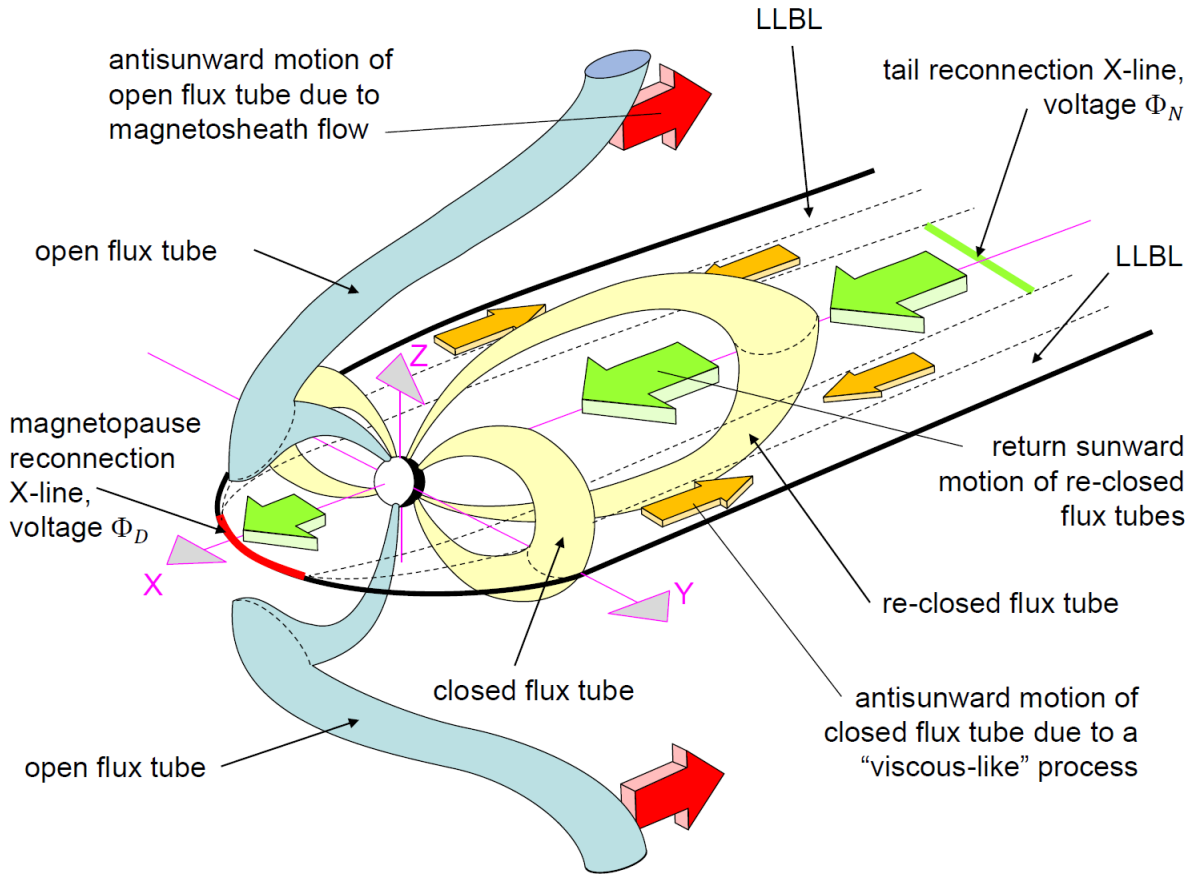

1061

1062 **Figure 1**. Schematic of the three convection drivers in the magnetosphere and ionosphere,
1063 adapted from *Cowley* (1982) with the addition of a reconnection X-line in the cross-tail
1064 current sheet (in green, the voltage across which is Φ_N) that re-closes open field lines and is
1065 included here because in the ECPC model (*Cowley and Lockwood*, 1992) it contributes to the
1066 ionospheric transpolar voltage Φ_{PC} at any one time by adding to the effect of the reconnection
1067 voltage Φ_D along the dayside magnetopause X-line (in red) which generates open field lines.
1068 The third source of Φ_{PC} is "viscous-like" momentum transfer across the magnetopause onto
1069 closed field lines that generates a total antisunward magnetic flux transfer of closed flux of
1070 voltage Φ_V in the low latitude boundary layers (LLBL).

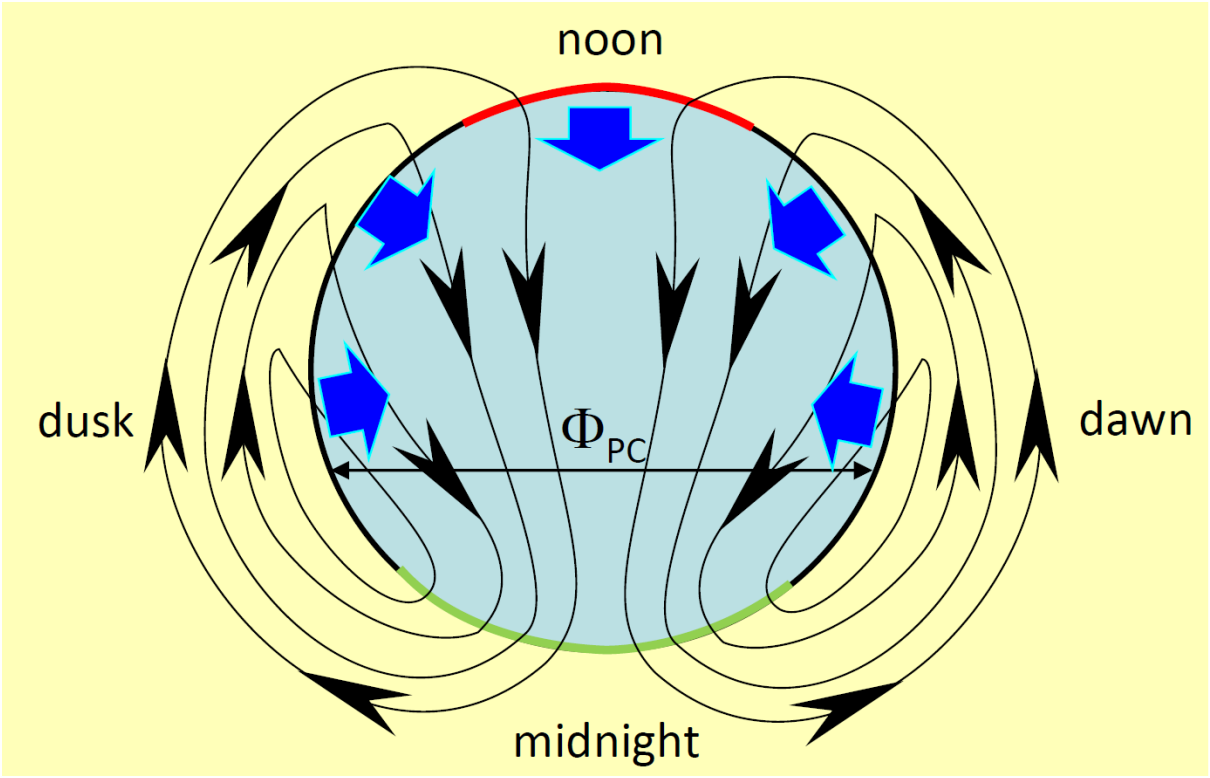

Figure 2. Schematic illustration of ionospheric flow streamlines (eqipotentials) under the influence of all three driving voltages Φ_D , Φ_N and Φ_V discussed in Figure 1, as predicted by the ECPC model of ionospheric flow excitation. This example of a contracting polar cap with $\Phi_N > \Phi_D$ is chosen because it illustrates how reconnection in the cross-tail current sheet can a imitate viscous-like proces – both in generating transpolar voltage Φ_{PC} while the IMF points northward and in the pattern of ionospheric flow on the dayside. This is dayside flow is driven by the contracting dayside polar cap boundary (blue arrows) which gives poleward flow with streamlines crossing the open-closed field line boundary, even though no reconnection is occurring, because plasma and field lines move with the "adiaroic" boundary (meaning "not flowing across") as it contracts (*Siscoe and Huang*, 1985).

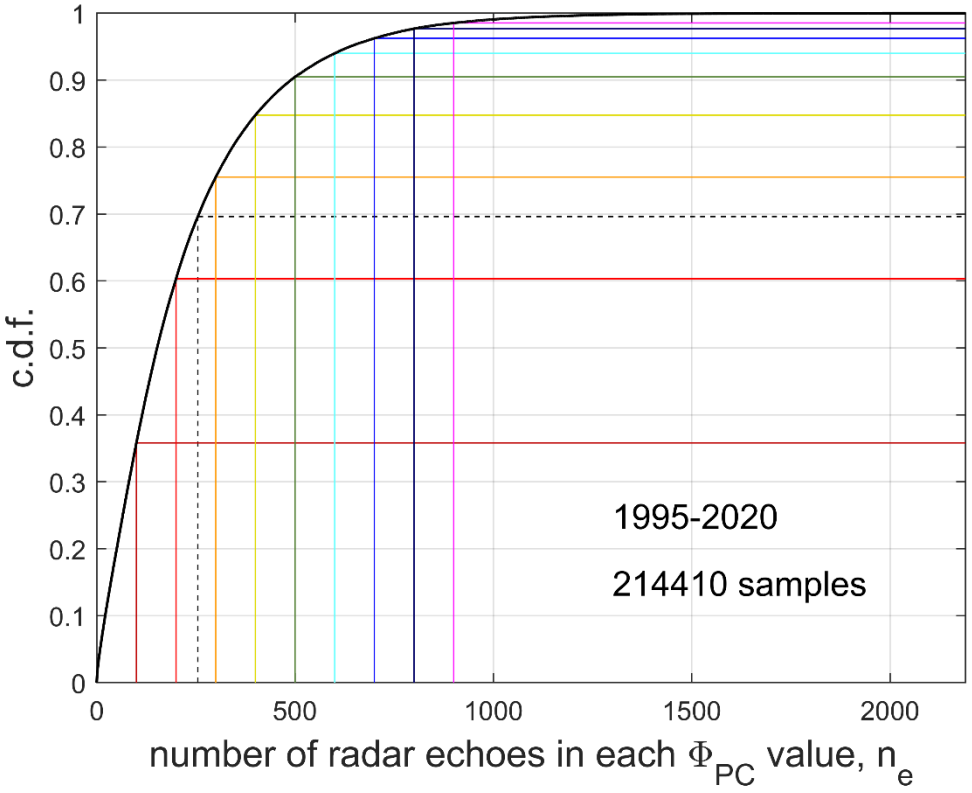

Figure 3. Cumulative probability distribution of the number of radar echoes, n_e, used in compiling the convection patterns, and hence the transpolar voltage Φ_{PC} estimates in the dataset employed here of 214410 Φ_{PC} values obtained from the SuperDARN radar array using the matched potential technique between 1995 and 2020. The vertical lines are various threshold values used in this paper which n_e must exceed for the Φ_{PC} value obtained to be considered valid. The black dashed line is at n_e = 255 which was found to be optimum in a comparison with 2-years data from satellite passes (2001-2002) and which yields $N = 60653$ valid Φ_{PC} estimates which is close to 30% of all observations. The coloured lines are for thresholds of [100:100:900] which are here used in a sensitivity study to understand the effect of the adopted threshold.

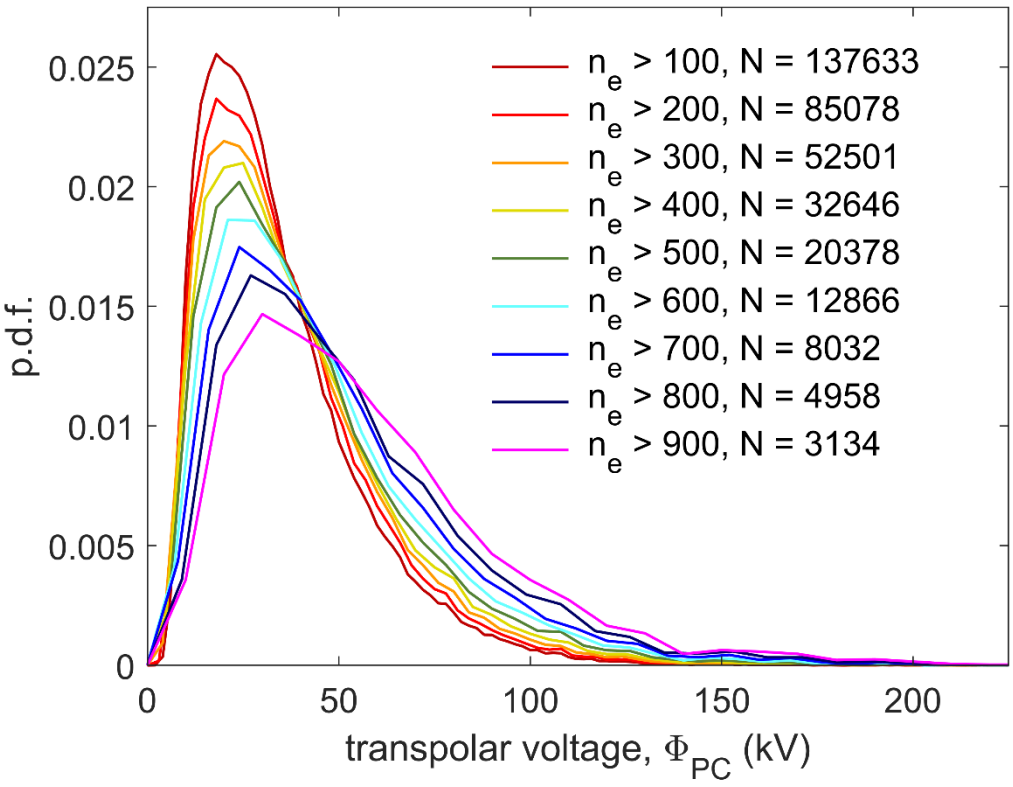

1093

1094 **Figure 4**. Probability density functions giving the distributions of the Φ_{PC} values for
1095 threshold values for the number of echoes n_e required of [100:100:900]. The resulting total
1096 number of Φ_{PC} values in the data set meeting that requirement, N, is given in each case.

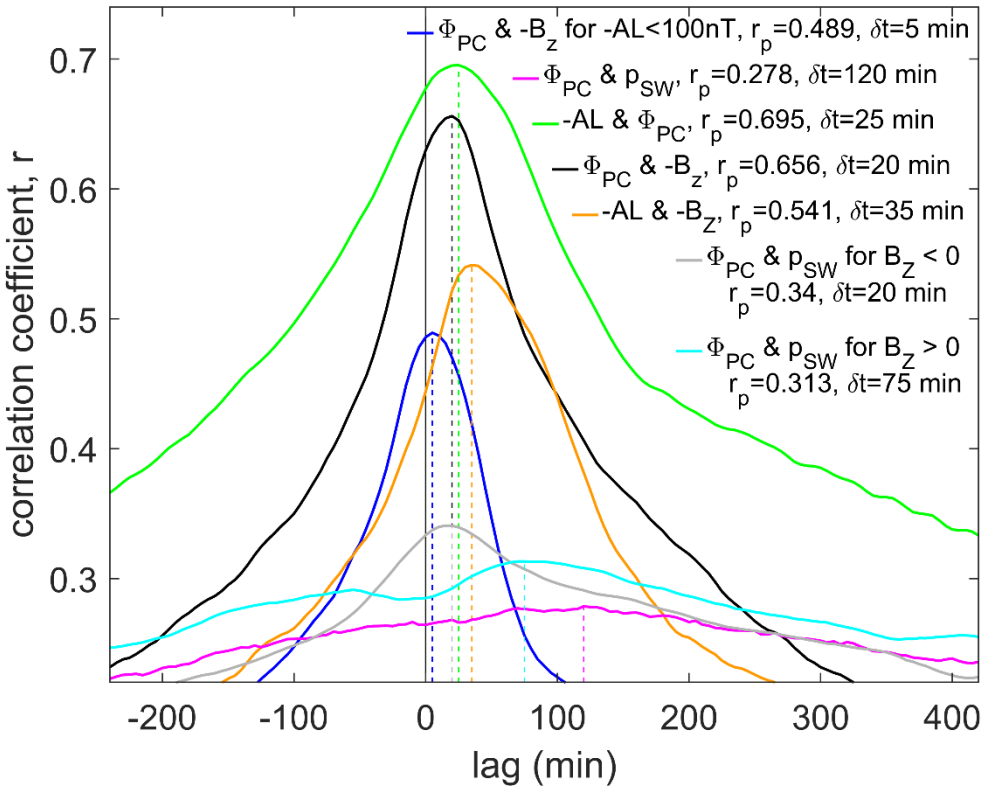

Figure 5. Lag correlograms used to determine the optimum lags δt: (black) for Φ_{PC} and IMF $-B_Z$ (in the GSM frame); (blue) for Φ_{PC} and IMF $-B_Z$ (in the GSM frame) for the subset with $-AL < 100nT$; (orange) for the $-AL$ index and IMF $-B_Z$; (green) the $-AL$ index and Φ_{PC}; (mauve, grey and cyan) for Φ_{PC} and the solar wind dynamic pressure p_{SW}: mauve is for all data, grey for southward IMF ($B_Z < 0$) and cyan for northward IMF ($B_Z > 0$). In each case, the first parameter of the pair has been lagged with respect to the second by the lag given by the x-axis. The vertical dashed lines are at the lag δt yielding maximum r, r_p, and the values for δt and r_p are given for each case in the legend. All data are selected by the Φ_{PC} dataset for $n_e > n_{lim} = 255$ radar echoes.

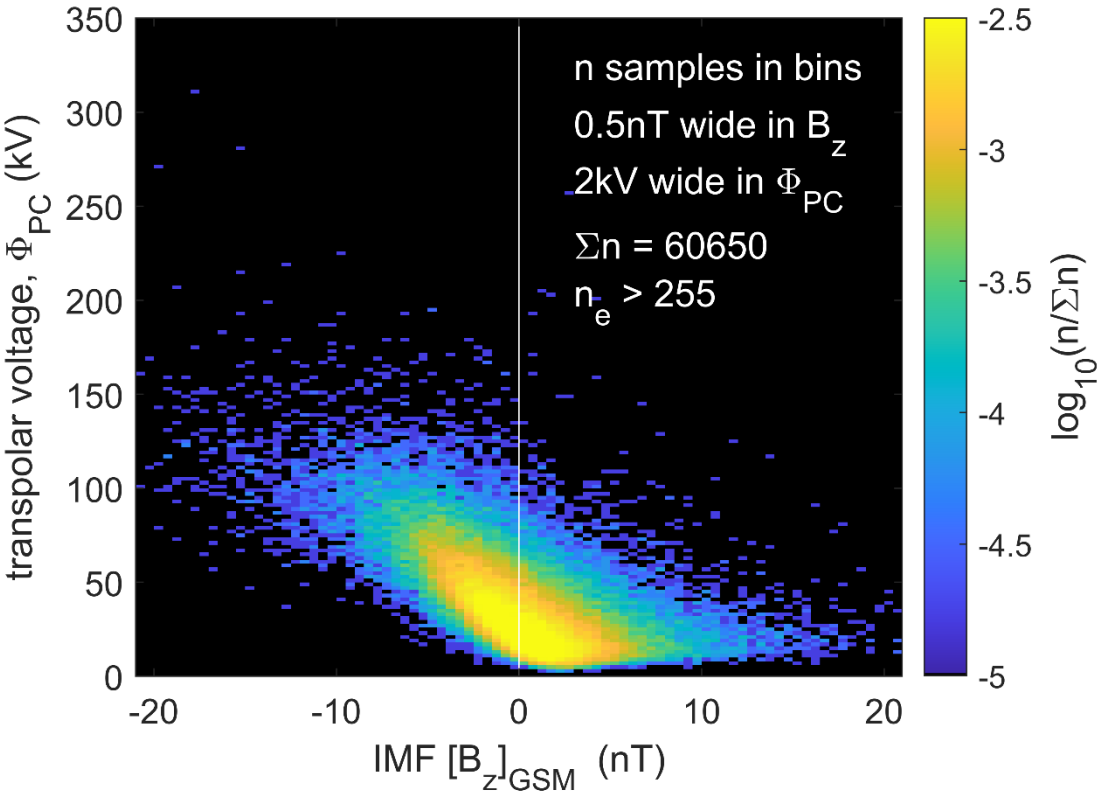

1107

1108 **Figure 6**. The fraction of samples $n/\Sigma n$ (on a logarithmic scale) in bins that are $\Delta B_z =$
1109 $0.5nT$ wide in IMF B_z (in the GSM frame of reference) and $\Delta\Phi_{PC} = 2\ kV$ wide in the Φ_{PC},
1110 as a function of B_z and Φ_{PC}. The IMF B_z data are 60-minute boxcar running means of 1-
1111 min. observations. Bins with no samples are shaded black. Only Φ_{PC} values based on $n_e >$
1112 $n_{lim} = 255$ radar echoes are used.

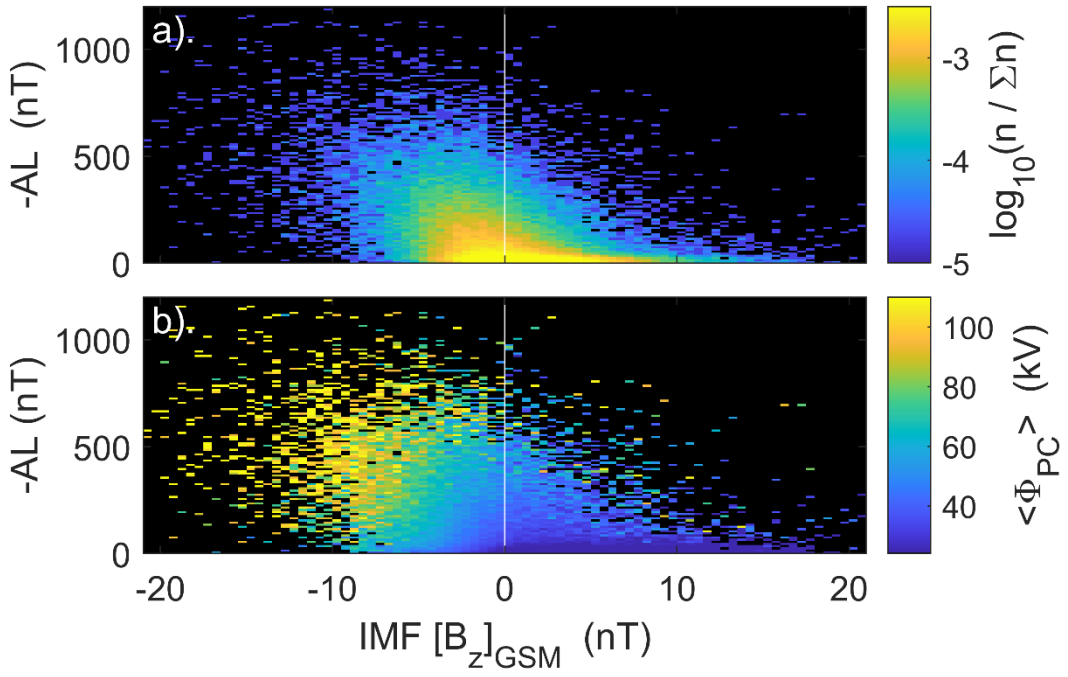

1113

1114 **Figure 7**. Plots of (a) the fraction of samples $n/\Sigma n$ (on a logarithmic scale) and (b) mean
1115 transpolar voltage $< \Phi_{PC} >$ in bins that are $\Delta B_z = 0.5nT$ wide in IMF B_z (in the GSM frame
1116 of reference) and $\Delta AL = 10\,nT$ wide in the AL index, as a function of B_z and $-AL$. Both of
1117 B_z and AL data are 15-minute boxcar running means of 1- minute observations. Bins with no
1118 samples are shaded black. Only Φ_{PC} values based on $n_e > 255$ radar echoes are used.

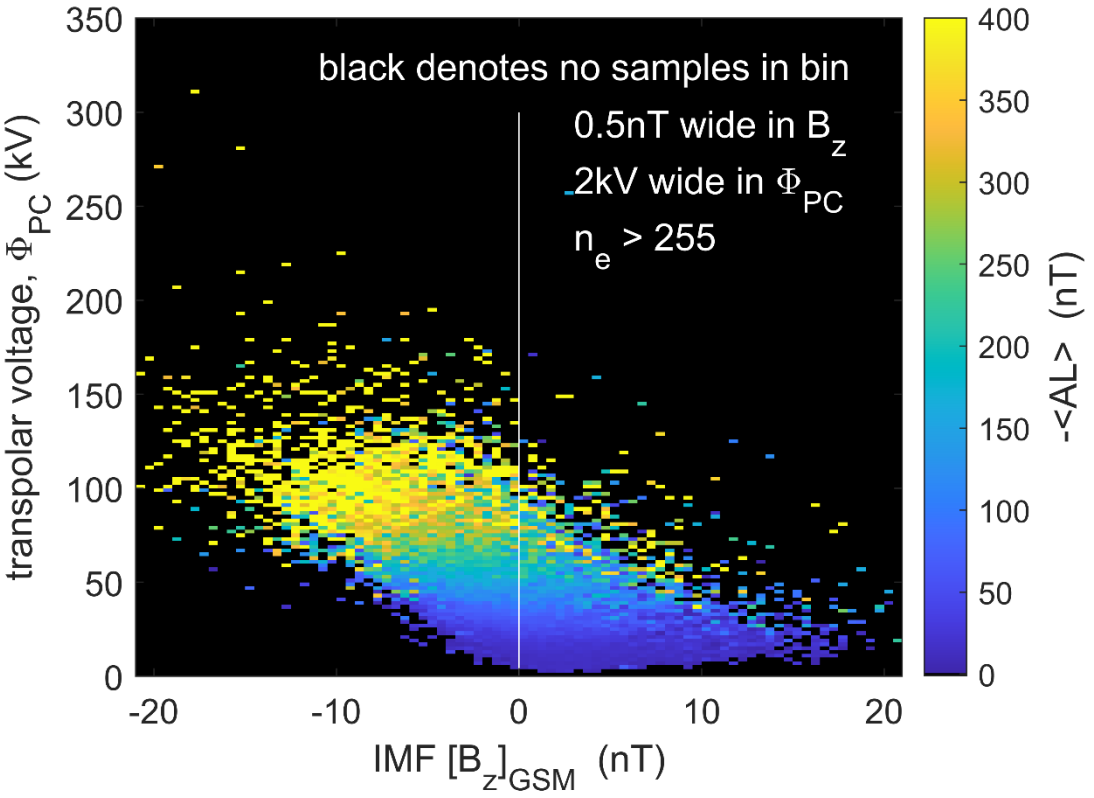

Figure 8. The same as Figure 5 for the mean negative AL index $-< AL >$. Bins with no samples are shaded black. Only Φ_{PC} values based on $n_e > 255$ radar echoes are used.

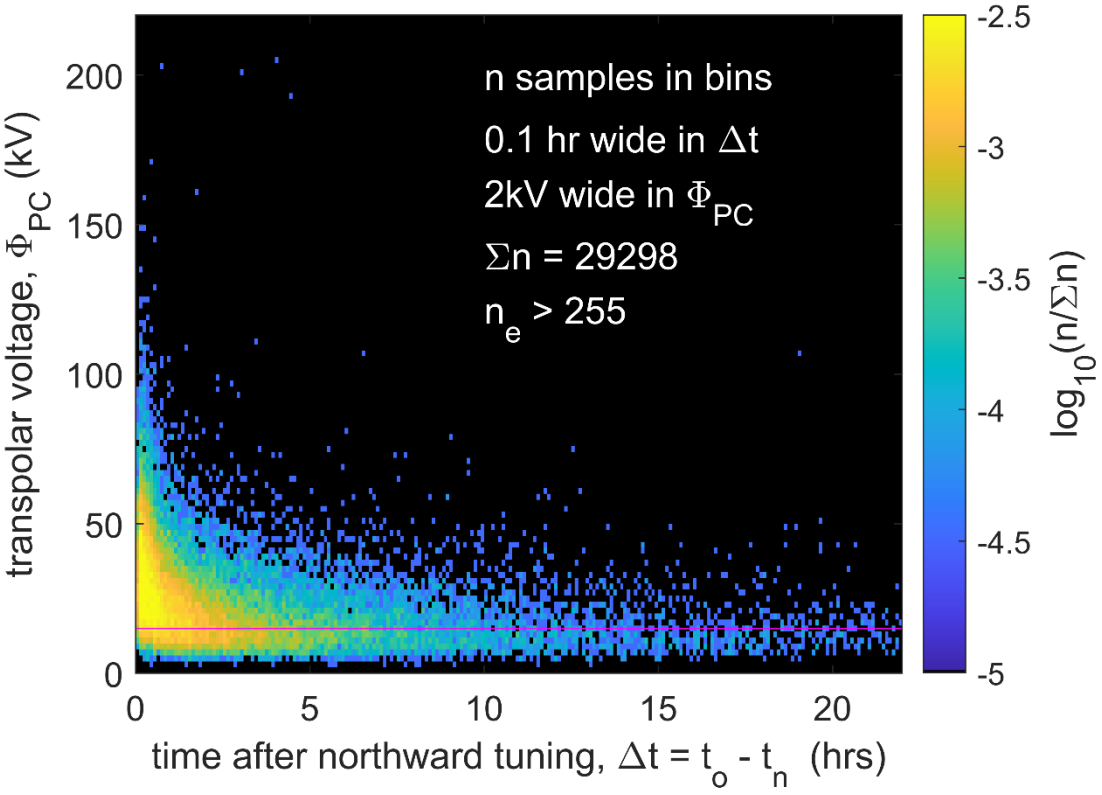

1122

1123 **Figure 9**. The fraction of samples $n/\Sigma n$ (on a logarithmic scale) during continuous
1124 northward IMF ($B_z > 0$ in the GSM frame of reference, using 15-minute boxcar running
1125 means of 1-minute IMF data) as a function of Φ_{PC} and the time that the IMF has been
1126 northward, $\Delta t = (t_o - t_n)$, where t_o is the time of the Φ_{PC} observation and t_n is the time at
1127 which the IMF turned northward in bins that are $0.1hr$ wide in Δt and 2 kV wide in Φ_{PC}.
1128 Bins with no samples are shaded black. Only Φ_{PC} values based on $n_e > 255$ radar echoes are
1129 used.

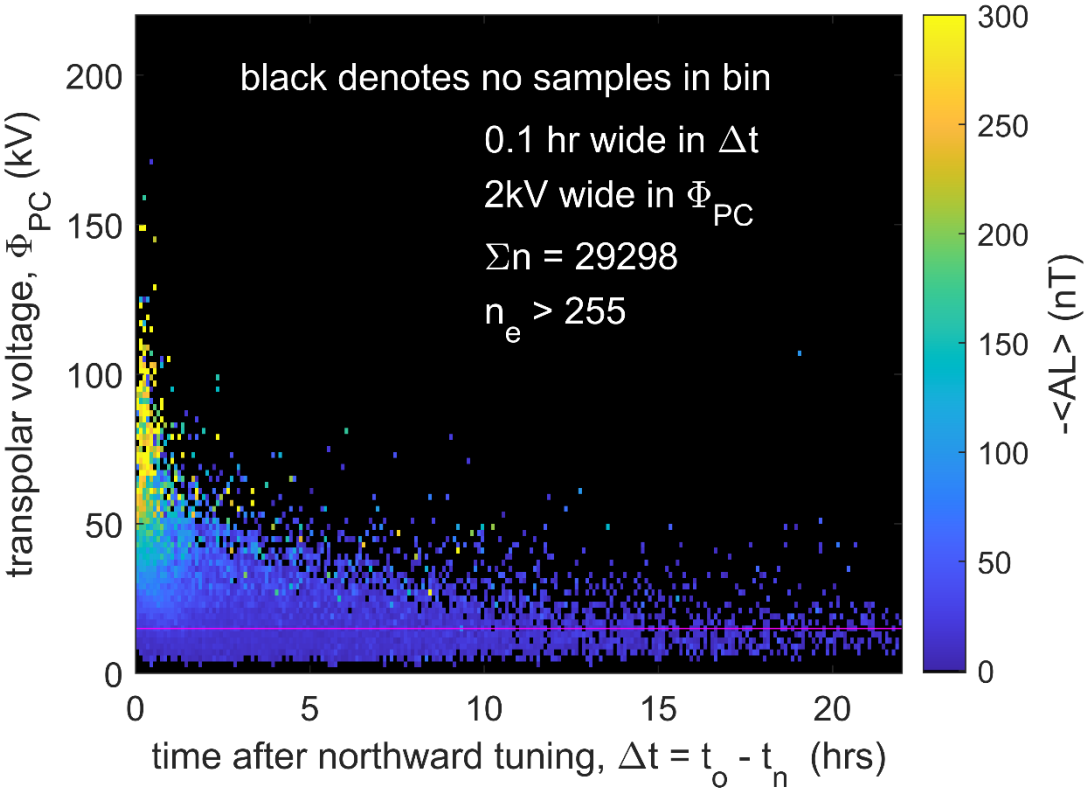

1130

1131 **Figure 10**. The same as figure 8 for the mean negative AL index $-< AL >$. Bins with no
1132 samples are shaded black. Only Φ_{PC} values based on $n_e > 255$ radar echoes are used.

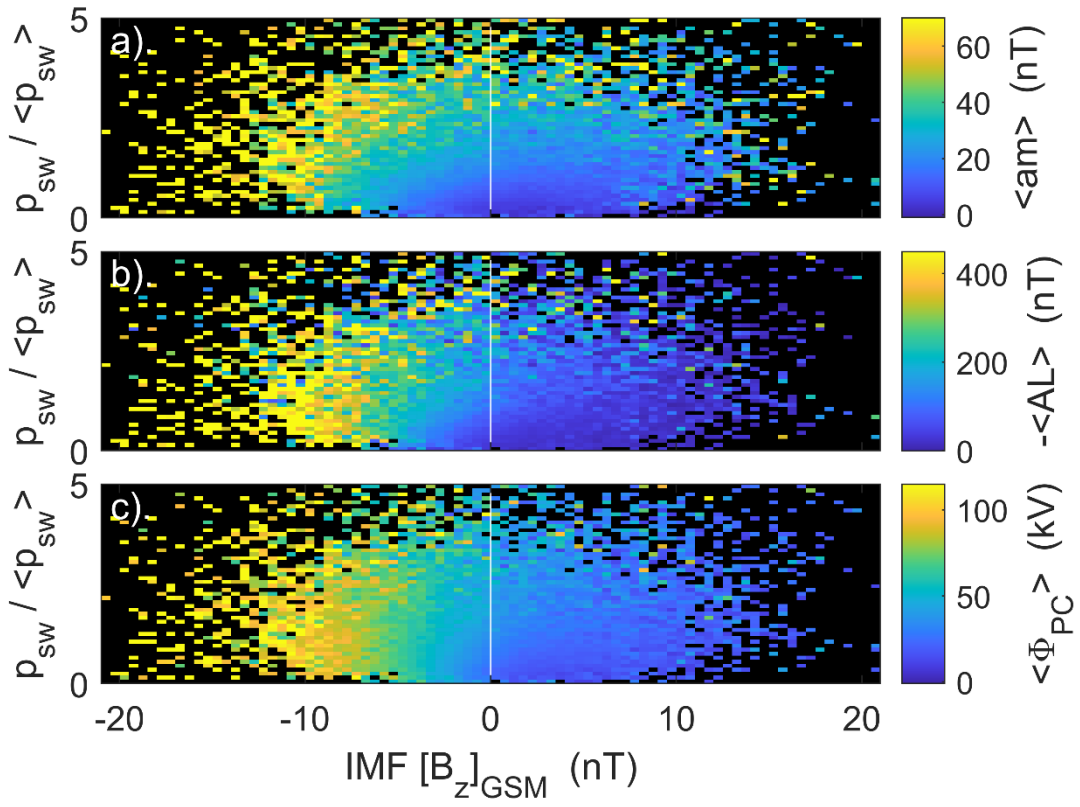

Figure 11. Plots mean values of (a) the am geomagnetic range index, (b) the mean negative AL index and (c) the mean transpolar voltage Φ_{PC} as a function of the northward IMF component (B_z) in the GSM frame of reference and the normalised solar wind dynamic pressure, $p_{SW}/< p_{SW} >$, where $p_{SW} = m_{SW}N_{SW}V_{SW}^2$ and m_{SW} is the mean ion mass, N_{SW} the number density and V_{SW} the speed of the solar wind (the normalising factor $< p_{SW} >$ is the mean for all data in the 1995-2020 period of this study). The AL, Φ_{PC}, and p_{SW} are all 15-minute boxcar running means of 1-minute data whereas the am data are linearly interpolated to the time of the Φ_{PC} sample from the raw 3-hourly am data. Bins are $\Delta B_z = 0.5nT$ wide in IMF B_z and 0.1 wide in $p_{SW}/< p_{SW} >$. Bins with no samples are shaded black. The am, $-AL$, and Φ_{PC} values used were for times of Φ_{PC} samples that are based on $n_e > 255$ radar echoes.

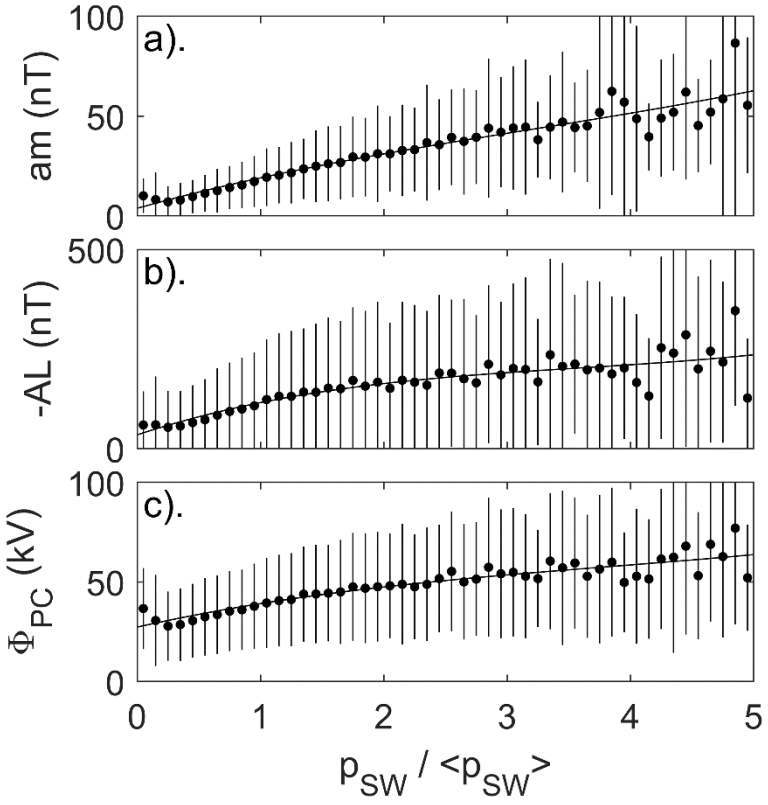
a).
b).
c).
am (nT)
-AL (nT)
Φ_{PC} (kV)
100
50
0
500
0
1
2
3
4
5
p_{SW} / <p_{SW}>
1145

1146 **Figure 12**. Mean values (with uncertainty bars of plus and minus one standard deviation) of
1147 (a) the am geomagnetic range index, (b) the negative AL index and (c) the transpolar voltage
1148 Φ_{PC} as a function of the normalised solar wind dynamic pressure $p_{SW}/< p_{SW} >$ in bins that
1149 are 0.1 wide in $p_{SW}/< p_{SW} >$. The am, $-AL$, and Φ_{PC} values used were for times of Φ_{PC}
1150 samples that are based on $n_e > 255$ radar echoes.

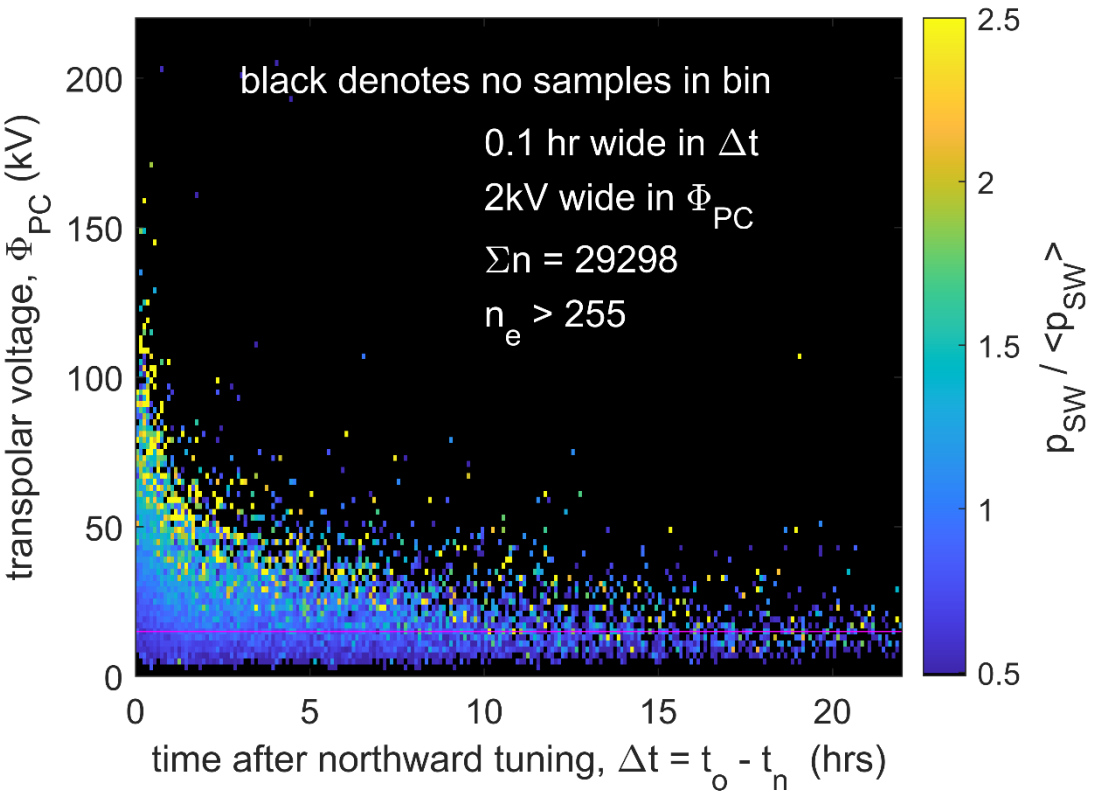

1151

1152 **Figure 13**. Same as Figure 9 for the normalised solar wind dynamic pressure, $p_{SW}/< p_{SW} >$.

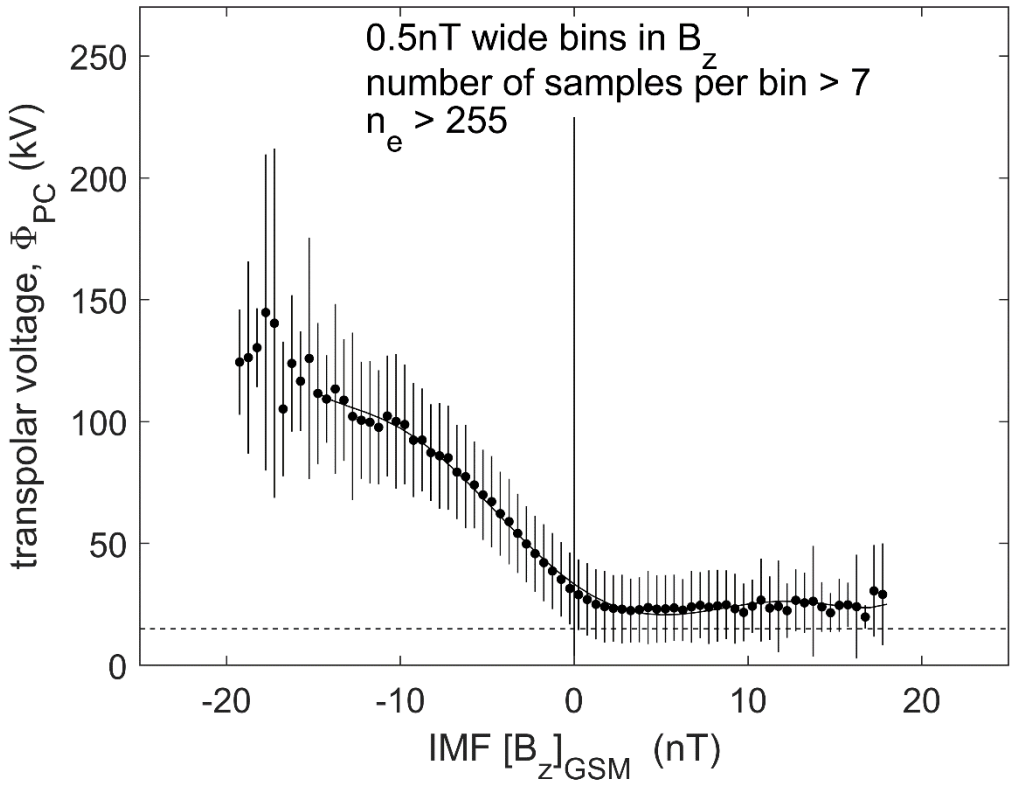

1153

1154 **Figure 14**. Mean values (with uncertainty bars of plus and minus one standard deviation) of
1155 the transpolar voltage Φ_{PC} as a function of IMF B_z (in the GSM frame of reference) in bins
1156 that are $\Delta B_z = 0.5nT$ wide for Φ_{PC} samples that are based on $n_e > 255$ radar echoes. The
1157 solid line is a 6th-order polynomial fit to the mean values.

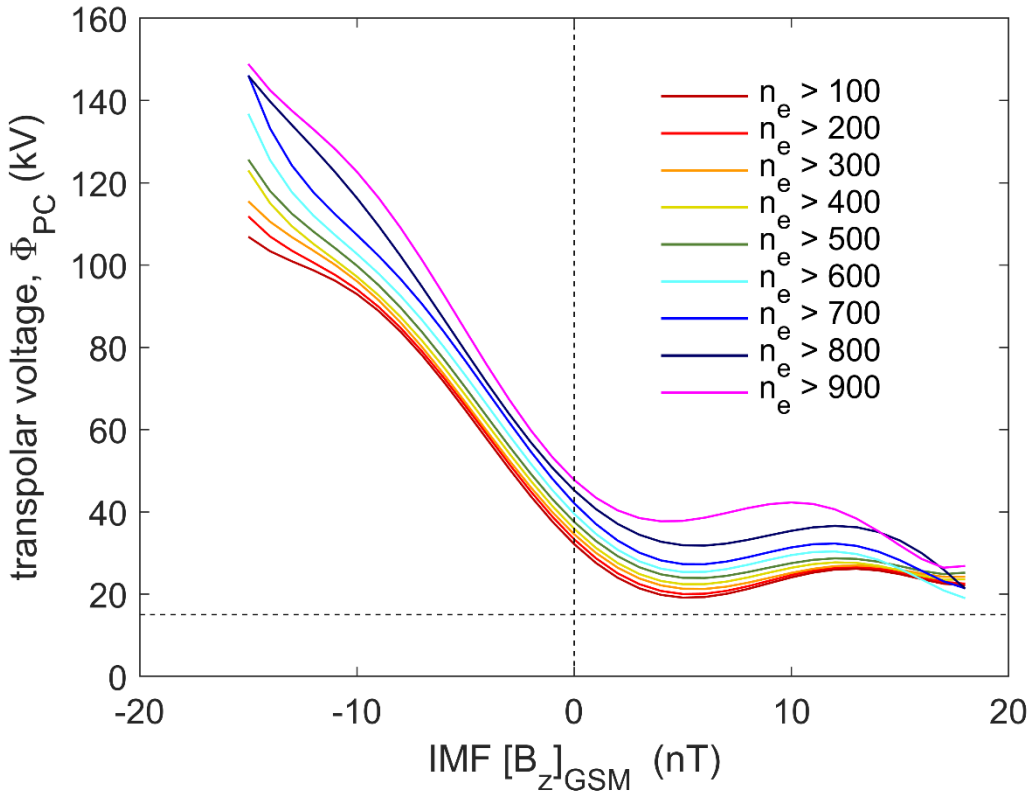

1158

1159 **Figure 15**. Analysis of the effect on figure 12 of the threshold required for the number of
1160 radar echoes, n_e. The coloured lines are 6th-order polynomial fits to the mean values of Φ_{PC}
1161 for n_e thresholds of [100:100:900] that were also used in Figures 3 and 4.

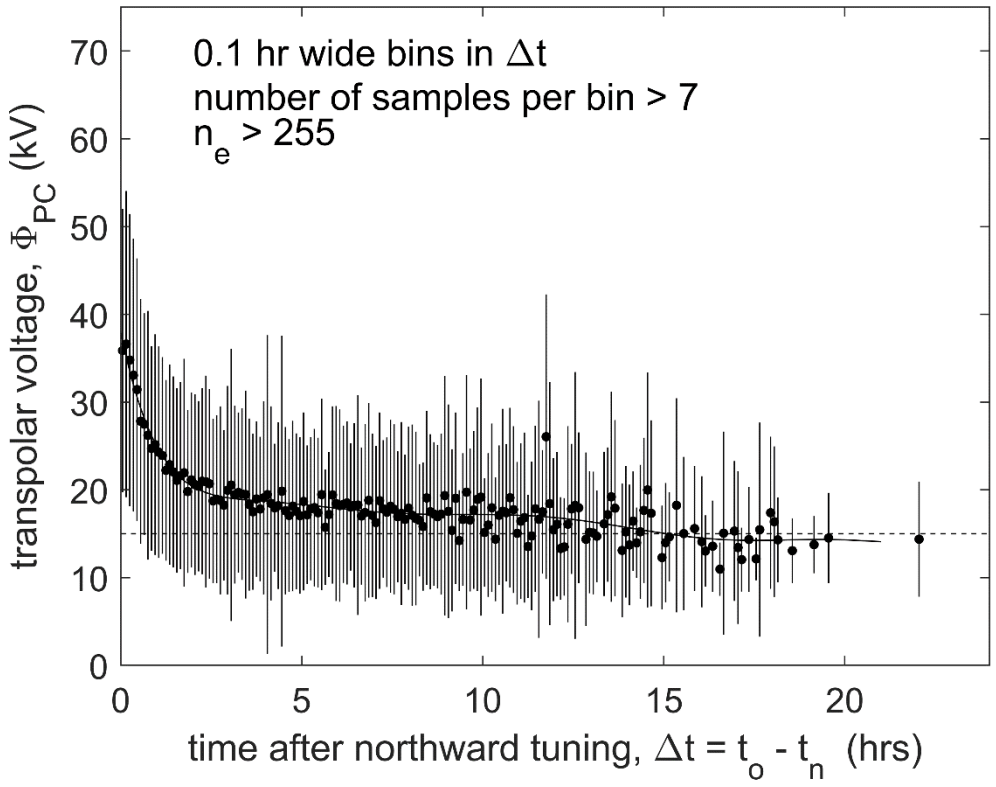

Figure 16. Mean values (with uncertainty bars of plus and minus one standard deviation) of the transpolar voltage Φ_{PC} during northward IMF as a function of time since the IMF turned northward $\Delta t = (t_o - t_n)$ in bins that are $0.1hr$ wide where t_o is the time of the Φ_{PC} observation and t_n is the time at which the IMF turned northward. Φ_{PC} samples are based on $n_e > 255$ radar echoes. The solid line is a 6th-order polynomial fit to the mean values.

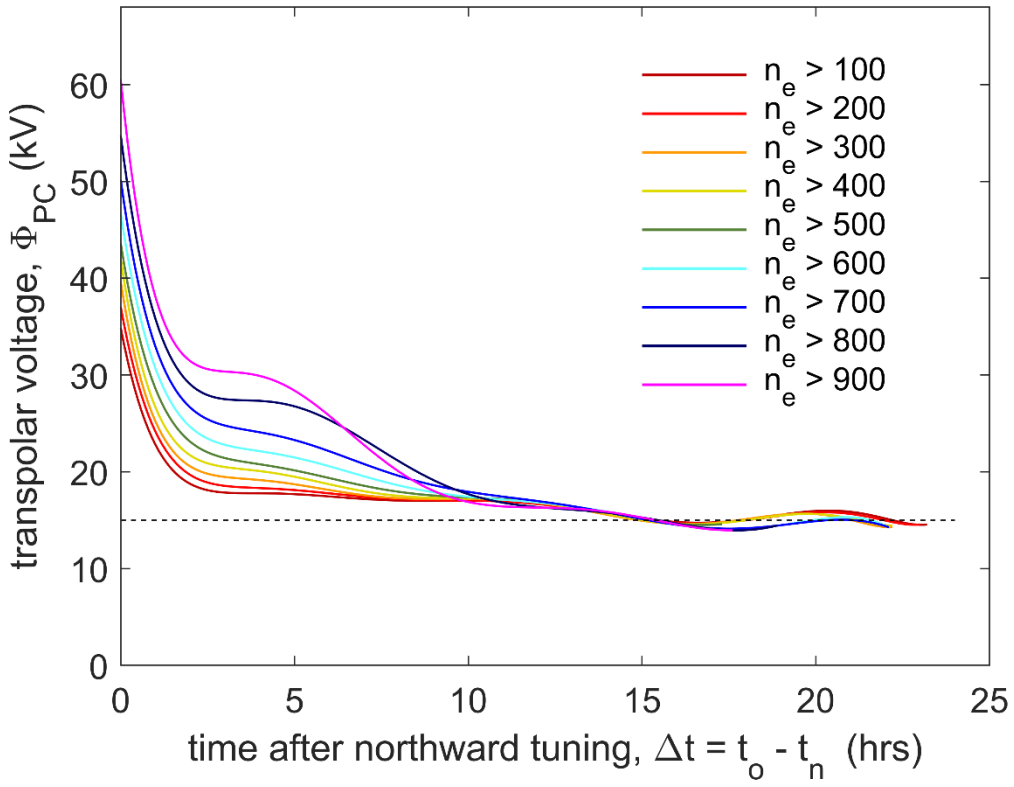

1168

1169 **Figure 17**. Analysis of the effect on figure 14 of the threshold required for the number of
1170 radar echoes, n_e. The coloured lines are 6th-order polynomial fits to the mean values of Φ_{PC}
1171 for n_e thresholds of [100:100:900] that were also used in Figures 3, 4 and 13.

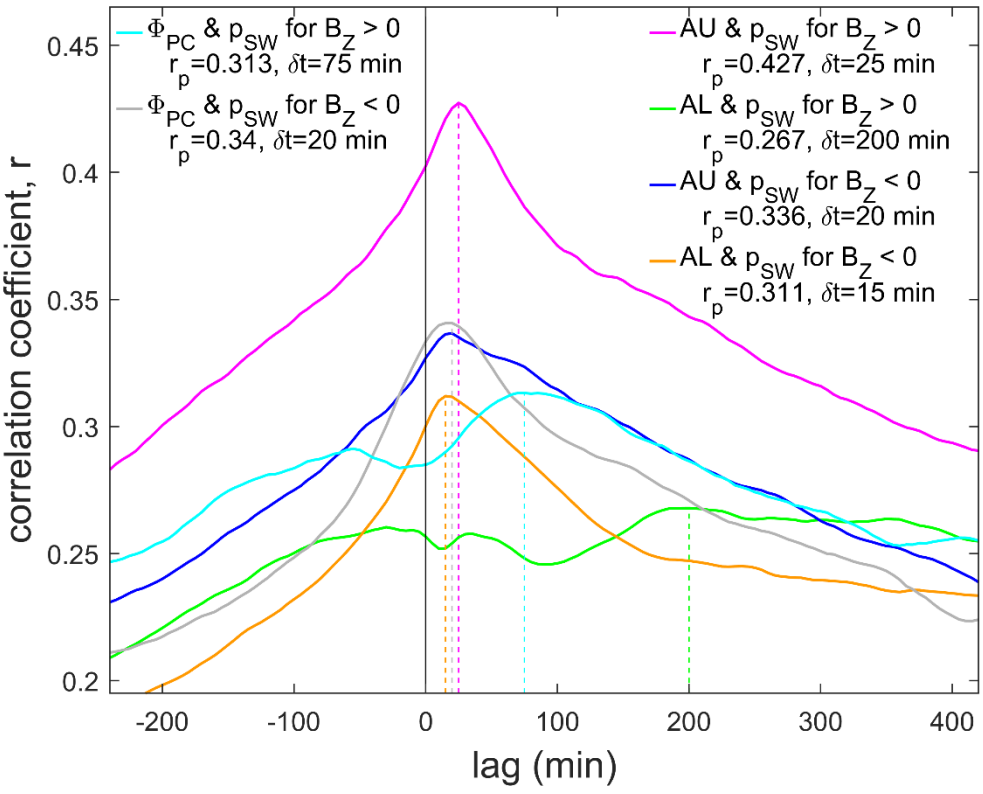

Figure 18. Lag correlograms for auroral electrojet indices with solar wind dynamic pressure (mauve) for AU and p_{SW} for IMF $B_Z > 0$ (in the GSM frame); (green) for AL and p_{SW} for IMF $B_Z > 0$; (blue) for AU and p_{SW} for IMF $B_Z < 0$; and (green) for AU and p_{SW} for IMF $B_Z < 0$. In each case, the first parameter of the pair has been lagged with respect to the second by the lag given by the x-axis. The vertical dashed lines are at the lag δt yielding maximum r, r_p, and the values for δt and r_p are given for each case in the legend.